Universität
Münster

Thorben Bruns

› Constraints on First-Order Phase Transition Parameters in the Early Universe

04.09.2025

living.knowledge

Constraints on First-Order Phase Transition Parameters in the Early Universe

Bachelor thesis
submitted to the

Universität Münster
Institute for Theoretical Physics

by

Thorben Bruns

04.09.2025

First examiner:	Jun.-Prof. Dr. K. Schmitz
Second examiner:	Prof. Dr. J. Heitger
Day of submission:	04.09.2025

Abstract

This Bachelor's thesis investigates first-order phase transitions (FOPTs) in the early Universe as a potential source of the nanohertz stochastic gravitational-wave background (SGWB), for which pulsar timing arrays (PTAs) have reported strong evidence. An FOPT proceeds via nucleation, expansion, and collision of bubbles of the new phase, processes that can generate gravitational waves (GWs). Using the `PTArcade` framework with the NANOGrav 15-year dataset, we fit theoretical templates to the GW spectra from the three mechanisms that are generically present in FOPTs: bubble collisions, sound waves and magnetohydrodynamic (MHD) turbulence, with each template treating at least one of these contributions as dominant. We describe each spectrum either by thermodynamic parameters (e.g. H_*R_*, T_*) or by geometric parameters (e.g. peak amplitudes and frequencies) and aim to constrain the corresponding parameter sets.

Our results indicate that the PTA-inferred nanohertz SGWB can be plausibly explained by energetic FOPTs occurring at temperatures $T_* \sim 100\,\text{MeV} - 1\,\text{GeV}$, with large kinetic-energy fractions ($K, \tilde{K} \to 1$) and bubble sizes approaching the Hubble horizon (i.e. $H_*R_* \sim 1$). Model-dependent differences arise: the first template, viewing bubble collisions as the main contribution, favors $\tilde{K} \approx 1$ and larger H_*R_*. The other two models, one emphasizing sound waves, the other sound waves with additional turbulence, prefer systematically lower T_* and H_*R_*, while the turbulence fraction ε, the bubble wall velocity v_w and high-frequency slopes remain largely unconstrained. Including a supermassive black-hole binary (SMBHB) foreground relaxes some constraints but does not qualitatively alter these conclusions. These findings motivate the application of the implemented models to next-generation PTA datasets to obtain more precise constraints on the thermodynamics of FOPTs in the early Universe.

Declaration of Academic Integrity

I hereby confirm that this thesis, entitled *Constraints on First-Order Phase Transition Parameters in the Early Universe*, is solely my own work and that I have used no sources or aids other than the ones stated. All passages in my thesis for which other sources, including electronic media, have been used, be it direct quotes or content references, have been acknowledged as such and the sources cited. I am aware that plagiarism is considered an act of deception which can result in sanction in accordance with the examination regulations.

I consent having my thesis cross-checked with other texts to identify possible similarities and to having it stored in a database for this purpose.

I confirm that I have not submitted the following thesis in part or whole as an examination paper before.

Münster, 04.09.2025

Thorben Bruns

Contents

1 Introduction

In 1916, Albert Einstein predicted the existence of gravitational waves (GWs) as a consequence of his theory of general relativity [1]. After indirect evidence was found in the 1970s through the observed orbital decay of the Hulse–Taylor binary pulsar [2], the first direct detection of GWs from merging black holes was made by LIGO in 2015 [3] and the first direct detection from merging neutron stars was made by the LIGO and Virgo detectors in 2017 [4].

Even more recently, the Australian [5], Chinese [6], European [7], Indian, North American [8] and South African (MeerKAT) [9] pulsar timing array (PTA) collaborations reported, at varying levels, evidence for the presence of a nanohertz stochastic gravitational wave background (SGWB), possibly originating from supermassive black hole binaries (SMBHBs) or early-universe processes. A comparison of published individual PTA results by the International Pulsar Timing Array (IPTA) found no significant differences in the inferred SGWB parameters (agreement within 1σ). This comparison, however, is based on the published datasets available at the time (IPTA DR2 / earlier PTA releases) and therefore does not yet include some of the more recent PTA datasets mentioned above. These newer releases (e.g. the NANOGrav 15-yr dataset) are planned to be incorporated in the upcoming IPTA DR3, which is expected to provide improved sensitivity and broader pulsar coverage. Consistent evidence across the collaborations further supports the interpretation that the various PTAs are observing an SGWB [10].

PTAs aim to detect an SGWB by identifying a characteristic spatial correlation pattern in the timing residuals of pulsar pairs, described by the so-called overlap reduction function (ORF). In general relativity, the ORF for an isotropic, unpolarized

SGWB is given by the Hellings–Downs curve.
Pulsars are rapidly rotating neutron stars that emit radiation along their magnetic field axes. Due to their rotational stability, they act like highly precise cosmic clocks [11]. Therefore, GWs can be detected by observing slight variations in the arrival times of their pulses caused by the passing waves.

This work is focused on exploring one possible source for such an SGWB: First-order phase transitions (FOPTs). A first-order phase transition in the early universe refers to a process in which the universe changed from one vacuum state to another through the formation of bubbles of the new phase. These bubbles nucleate, expand, and eventually collide, completing the transition. The process is discontinuous, involving a latent heat release. The discovery of GWs from FOPTs could help explain the matter-antimatter asymmetry, depending on the specifics of the phase transition, since FOPTs are out-of-thermal-equilibrium processes that may satisfy one of the Sakharov conditions for baryogenesis, and in some scenarios could also be linked to the existence of dark matter [12].

The main goal of this project is to constrain the parameters of generic FOPTs (i.e., thermodynamic and geometric parameters) in the early universe by fitting the templates for the shape of the GW spectrum following [13] to the NANOGrav 15 year data [14].
This thesis is structured as follows: chapter 2 presents the theoretical background on FOPTs, GWs and the SGWB, including the foundation of PTAs and a discussion of the Hellings–Downs curve, which encodes the expected spatial correlations induced by an SGWB. chapter 3 discusses the generation of GWs specifically by FOPTs. chapter 4 introduces `PTArcade`, a wrapper for the PTA analysis software `enterprise`, which is used to fit the spectral templates to the data. chapter 5 presents and discusses the results, specifically cornerplots for different phase transition models and parameters. Finally, chapter 6 provides a summary and outlook.

Theoretical Background

2

2.1 First-Order Phase Transitions

This section introduces the principles behind FOPTs, starting with general concepts of phase transitions (PTs) in the early universe and when they occurred in the context of cosmology. The focus then shifts to a detailed explanation of FOPTs and how they are related to symmetry breaking. This chapter is based on Ref. [12].

In the context of cosmology, a phase transition refers to a process in which the bulk properties of the early universe undergo significant changes over a relatively short period of time. An analogous everyday example would be the phase changes of water once it heats up or cools down. It is believed that during the expansion and cooling of the universe one or more PTs occurred. The two currently known early universe PTs are the quantum chromodynamics PT (QCD PT) and the electroweak PT (EW PT). In Figure 2.1 these PTs can be seen embedded in the history of the universe. The QCD PT happened at a temperature of roughly $0.1\ \mathrm{GeV}$ (seen in Figure 2.1 under "hadrons form") and the EW PT occurred at $100\ \mathrm{GeV}$, which is marked "EWSB" in Figure 2.1, short for *Electroweak Symmetry Breaking*. After reheating the universe contains a hot plasma of mostly quarks and gluons (marked "QGP" for *Quark Gluon Plasma*). Only at the QCD scale these particles combine to hadrons and the bulk properties of the vacuum change. This process is called the QCD PT. Before that transition, the Higgs particle gave mass to the particles of the SM, again changing the bulk properties, which classifies that process as a PT (the EW PT).

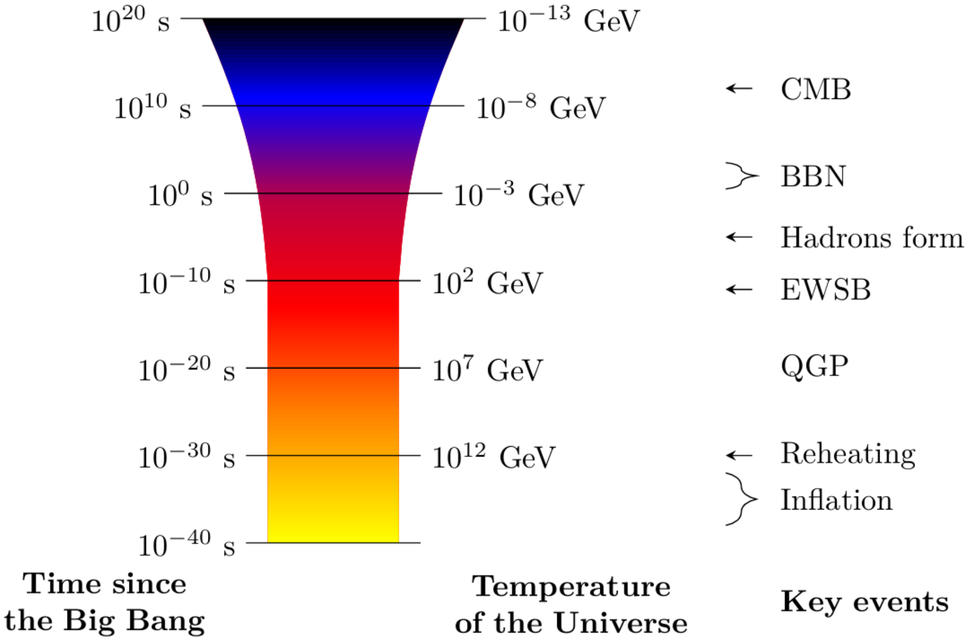

Figure 2.1: This figure shows the chronology of the universe. The time-temperature relation illustrated here is based on a radiation-dominated universe and assumes no extra particle species beyond those included in the Standard Model. The key events, especially the events leading to PTs are outlined in section 2.1. This figure is taken from Ref. [12].

2.1.1 Spontaneous Symmetry Breaking

Mathematically, a symmetry is defined as a feature that remains unchanged under a transformation. For example, the conservation of energy reflects an underlying symmetry of time translation, as described by Noether's theorem [15]. However, these symmetries can behave differently at different energy scales. While a system's vacuum can respect a certain symmetry at high energies, the vacuum state may no longer exhibit this symmetry as the energy decreases. This effect is called *spontaneous symmetry breaking* (SSB). A commonly studied example is the *Abelian Higgs model* in scalar electrodynamics. Its potential energy is given by:

$$V(\Phi) = -m^2\Phi^\dagger\Phi + \lambda(\Phi^\dagger\Phi)^2, \tag{2.1}$$

where Φ is a complex scalar field. This potential has a U(1) symmetry, meaning it remains unchanged under phase rotations of Φ. However, the minimum of the potential, the vacuum state, is not at $\Phi = 0$, but at a finite field value $|\Phi| = v$, where $v = \frac{m}{\sqrt{2\lambda}}$. This leads to a vacuum that does not respect the underlying symmetry, even though the theory itself does.

The shape of the potential resembles a "Mexican hat" or wine bottle (see Figure 2.2). It is symmetric around the origin, but with the lowest energy states forming a circle at non-zero radius. Choosing a vacuum state means selecting one specific point on this circle (choosing a certain phase), thereby "breaking" the symmetry spontaneously.

At finite temperatures, the potential changes. Thermal corrections modify the effective mass term of the field. The potential energy is now given by:

$$V(\Phi, T) = (-m^2 + T^2)\Phi^\dagger\Phi + \lambda(\Phi^\dagger\Phi)^2 \tag{2.2}$$

At high temperatures T, the symmetric state $\Phi = 0$ is energetically favored. As the universe cools down, the shape of the potential evolves and at a certain critical temperature ($T^2 < m^2$), the minimum shifts away from zero, breaking the symmetry. This transition of the vacuum state defines a PT and the order parameter is given by the vacuum value of Φ. The following Figure 2.2 shows the discussed concepts.

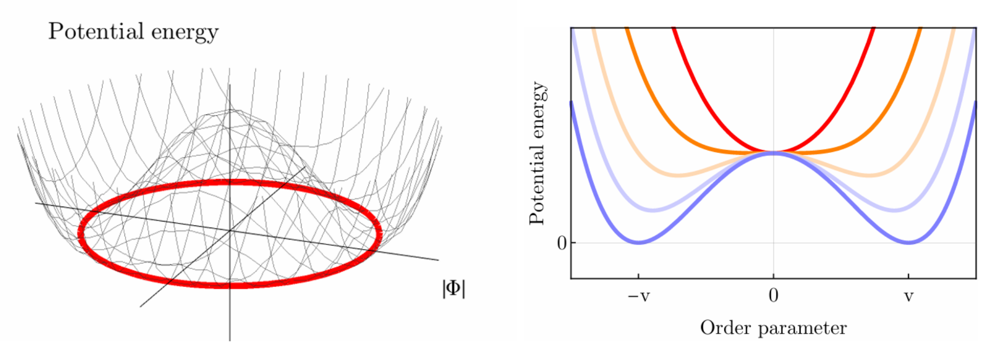

Figure 2.2: This figure illustrates the spontaneous symmetry breaking using the Abelian Higgs potential. The potential energy as a function of the complex field Φ is seen on the left. The red circle marks the vacuum.
The cross sections of the potential in Equation 2.2 at various temperatures is seen on the right. At high temperatures (red/orange), the minimum is at $\Phi = 0$, while at lower temperatures (blue), the vacuum lies away from zero, indicating spontaneous symmetry breaking. This figure is taken from Ref. [12].

Depending on the shape of the potential, the PT can be either continuous (second order) or discontinuous (first order). FOPTs are of special interest in cosmology, as they can release a significant amount of latent energy and lead to phenomena such as bubble nucleation. In such cases, the field does not smoothly roll into the new vacuum, but transitions via quantum tunneling or thermal fluctuations over a potential barrier. For example, the following potential features a FOPT due to the spontaneous breaking of a U(1) symmetry

$$V(|\Phi|, T) = \left(-m^2 + T^2\right) |\Phi|^2 - T|\Phi|^3 + \lambda|\Phi|^4. \tag{2.3}$$

For temperatures T in the range $m < T < 2m\sqrt{\lambda}/\sqrt{4\lambda - 1}$, the potential looks as in Figure 2.3. While the vacuum state of the potential is at $\Phi = 0$ for high temperatures, it becomes metastable once the temperature drops below a critical temperature. The vacuum changes discontinuously from the local minimum at $\Phi = 0$ (false vacuum) to the newly emerged global minimum (true vacuum). Due to the changes in the potential energies of the vacua, latent heat is released.

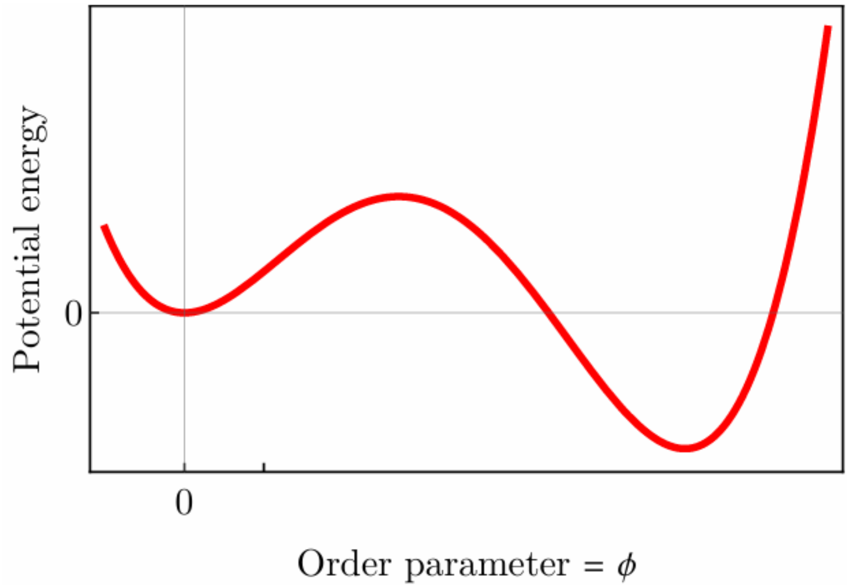

Figure 2.3: This figure shows the potential described in Equation 2.3 for $m < T < 2m\sqrt{\lambda}/\sqrt{4\lambda - 1}$. The two minima are separated by a barrier. This figure is taken from Ref. [12].

To conclude, a FOPT is characterized by a discontinuous change in the vacuum state, accompanied by the release of latent heat. This transition is a statistical process triggered by thermal fluctuations or quantum tunneling, which can induce the nucleation of bubbles. The discussion of the bubble formation is the focus of the next subsection.

2.1.2 Bubble Nucleation

During a FOPT, the system initially resides in a metastable vacuum state, the false vacuum. Due to quantum tunneling or thermal fluctuations, regions of the more stable true vacuum can spontaneously form. These regions are called ”bubbles” of true vacuum.

In non-relativistic quantum mechanics, the tunneling probability can be estimated using the semiclassical WKB approximation. If the particle’s energy E is lower than the potential $V(x)$ between two points x_0 and x_1, its wavefunction decreases exponentially in that region, leading to a suppressed tunneling probability. The tunneling rate can be approximated as

$$\Gamma_{\rm WKB} \propto \exp\left[-\int_{x_0}^{x_1} \sqrt{2m(V(x)-E)}\, dx \right].$$

An analogous approach, the so called *bounce method* [16, 17], exists in quantum field theory. Here, one works in Euclidean spacetime, where the system is described by the Euclidean action

$$S_E = \int d^d x_E \left[(\partial_{x_E}\phi)^2 + V(\phi, T) \right], \tag{2.4}$$

where d is the effective number of dimensions. For quantum tunneling at zero temperature, we set $d = 4$, while for thermal transitions $d = 3$ due to the compactification of the Euclidean time direction in thermal field theory. Via extremising the action and assuming spherical symmetry, the equations of motion for the field $\phi(r)$, where r denotes the radial distance, reduce to

$$\frac{d^2\phi}{dr^2} + \frac{d-1}{r}\frac{d\phi}{dr} = \frac{dV(\phi, T)}{d\phi}, \tag{2.5}$$

To solve these equations, we need to impose boundary conditions, e.g., ensuring finite energy at the origin and vanishing ϕ at infinity. The corresponding decay rate per unit volume is then given by

$$\Gamma(T) = A(T)\, e^{-S_E T^{d-4}}, \tag{2.6}$$

where typically $A(T) \sim T^4$ by dimensional analysis. As the temperature decreases, $S_E(T)/T$ becomes smaller, leading to an exponential increase in the nucleation rate.

Once nucleated, bubbles of the true vacuum begin to expand if they exceed a critical radius R_c. The pressure difference between the false and true vacuum, driven by the release of latent heat, provides an outward force on the bubble wall. However, this expansion is opposed by friction arising from interactions with the surrounding thermal plasma. A bubble will only grow if it surpasses the critical radius at which the driving force overcomes the plasma-induced friction (for more details, see Ref. [18]).

As the transition progresses, more bubbles nucleate and expand until they eventually collide. These collisions, as well as the hydrodynamic response of the plasma (in particular sound waves and turbulence, further discussed in chapter 3), can give rise to a stochastic background of gravitational waves. Such a signal, if detected, could offer a unique observational window into the early universe.
To illustrate this, we revisit Figure 2.1, which shows the timeline of the universe, including the cosmic microwave background (CMB). Notably, potential FOPTs, such as hypothetical extensions of the electroweak or QCD transitions, would have occurred well before the formation of the CMB. During that era, photons were still in thermal equilibrium, meaning no electromagnetic radiation from that epoch remains observable today. In contrast, GWs were never in thermal equilibrium and can therefore directly probe the early universe.
To understand how FOPTs can give rise to GWs, the next section introduces the theoretical description of GWs.

2.2 Gravitational Waves

In this section we review the derivation of GWs as perturbations of the spacetime metric. The derivation is based on [11] and follows the standard treatment as presented in the textbook by Maggiore [19]. As a starting point we introduce the Einstein field equations.

GWs arise as wave-like solutions to the Einstein field equations in the weak-field limit. These equations relate the curvature of spacetime to the energy-momentum tensor:

$$G_{\mu\nu} := R_{\mu\nu} - \frac{1}{2} R g_{\mu\nu} = 8\pi T_{\mu\nu}, \tag{2.7}$$

where $G_{\mu\nu}$ is the Einstein tensor, $R_{\mu\nu}$ is the Ricci tensor, R is the Ricci scalar, $g_{\mu\nu}$ is the metric tensor, and $T_{\mu\nu}$ is the energy-momentum tensor. We use natural units $G = c = 1$.

To study GWs we consider weak-field perturbations $h_{\mu\nu}$ around flat Minkowski spacetime (see Ref. [20, 21], as originally proposed by Einstein):

$$g_{\mu\nu} = \eta_{\mu\nu} + h_{\mu\nu}, \qquad |h_{\mu\nu}| \ll 1, \tag{2.8}$$

where $\eta_{\mu\nu} = \text{diag}(-1, 1, 1, 1)$ is the Minkowski metric. In this regime, the Einstein tensor can be linearized in $h_{\mu\nu}$. To leading order, this yields:

$$\begin{aligned} G_{\mu\nu} = \tfrac{1}{2}\big(&\partial_\mu \partial^\alpha h_{\alpha\nu} + \partial_\nu \partial^\alpha h_{\alpha\mu} - \partial_\mu \partial_\nu h - \Box h_{\mu\nu} \\ &+ \eta_{\mu\nu} \Box h - \eta_{\mu\nu} \partial^\alpha \partial^\beta h_{\alpha\beta}\big), \end{aligned} \tag{2.9}$$

where $h = \eta^{\mu\nu} h_{\mu\nu}$ is the trace and $\Box = \eta^{\mu\nu}\partial_\mu\partial_\nu$ is the flat spacetime d'Alembertian. To simplify this expression, the *trace-reversed perturbation* is defined:

$$\bar{h}_{\mu\nu} := h_{\mu\nu} - \frac{1}{2}\eta_{\mu\nu} h. \tag{2.10}$$

This implies $\bar{h} = -h$ and it follows:

$$G_{\mu\nu} = \frac{1}{2}\left(\partial_\mu \partial^\alpha \bar{h}_{\alpha\nu} - \Box \bar{h}_{\mu\nu} + \partial_\nu \partial^\alpha \bar{h}_{\alpha\mu} - \eta_{\mu\nu} \partial^\alpha \partial^\beta \bar{h}_{\alpha\beta}\right). \tag{2.11}$$

Now choosing the *Lorenz gauge*, which can be reached via coordinate transformations of the form $x^\mu \to x^\mu + \xi^\mu$, imposes the condition:

$$\partial^\nu \bar{h}_{\mu\nu} = 0. \tag{2.12}$$

In this gauge, the Einstein equations simplify to:

$$\Box \bar{h}_{\mu\nu} = -16\pi T_{\mu\nu}. \tag{2.13}$$

In vacuum ($T_{\mu\nu} = 0$), one finds:

$$\Box \bar{h}_{\mu\nu} = 0, \tag{2.14}$$

which is a wave equation for each component of $\bar{h}_{\mu\nu}$, whose general solution describes plane waves propagating at the speed of light.

TT Gauge and Degrees of Freedom

Although $h_{\mu\nu}$ is a symmetric 4×4 tensor with 10 independent components, the gauge freedom allows to eliminate 4 components via the Lorenz gauge and 4 more by residual gauge transformations maintaining the Lorenz condition. This leaves only 2 physical degrees of freedom.

These correspond to the two polarization states of GWs. By choosing the *transverse-traceless (TT) gauge*, we impose the following:

$$h^{0\mu} = 0, \qquad \partial^j h_{ij} = 0, \qquad h^i_{\ i} = 0. \tag{2.15}$$

With these conditions the (TT) gauge, together with the Lorenz gauge, removes all non-radiative and gauge degrees of freedom.

In this gauge, a plane wave traveling in the z-direction has the form:

$$h^{\mathrm{TT}}_{\mu\nu}(t,z) = \begin{pmatrix} 0 & 0 & 0 & 0 \\ 0 & h_+ & h_\times & 0 \\ 0 & h_\times & -h_+ & 0 \\ 0 & 0 & 0 & 0 \end{pmatrix} \cos[\omega(t-z)], \tag{2.16}$$

where h_+ and $h_\times$ are the amplitudes of the two polarizations, the “plus” and “cross” modes. These describe tidal deformations of test masses in the plane transverse to the wave’s direction of propagation.

From Equation 2.16 we observe that the $+$-polarization stretches distances along the x-axis while simultaneously compressing them along the y-axis. The effect of the $\times$-polarization is analogous, but rotated by $\pi/4$ radians counterclockwise within the xy-plane. This tidal deformation, occurring in the plane perpendicular to the wave’s direction of propagation, is illustrated over a full wave cycle in Figure 2.4.

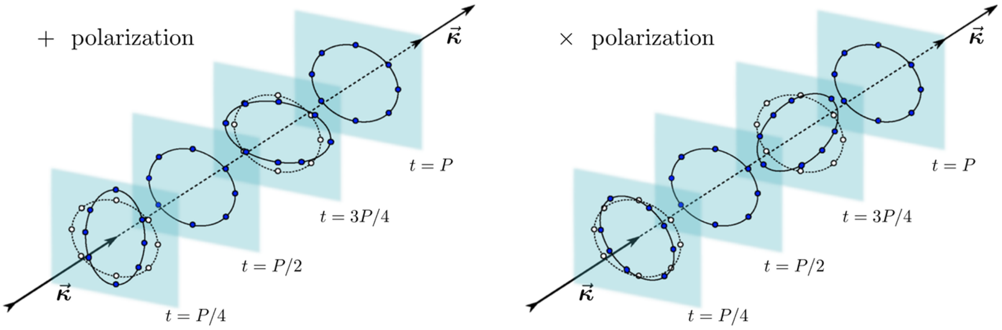

Figure 2.4: This figure illustrates the periodic deformation of spacetime caused by a gravitational wave, showing the two distinct polarization states allowed by general relativity. The deformation occurs entirely in the plane perpendicular to the wave's direction of propagation. Taken from Ref. [11].

To summarize, GWs emerge naturally as wave-like solutions to the Einstein field equations in the weak-field regime. It was shown how these waves influence the motion of test particles, illustrating their physical significance.
The next logical step is to study explicit solutions of the linearized wave equation (Equation 2.13) in order to gain insight into the types of processes that can generate gravitational radiation. This will be the focus of the following subsection, where we discuss the quadrupole formula.

2.2.1 The Quadrupole Formula

In this subsection, we follow the general approach of Ref. [12]. It turns out Equation 2.13 can be solved using the retarded Green's function. In particular, when the observer is located far from the source and the internal motions within the source are slow compared to the speed of light (i.e., non-relativistic velocities, $v \ll c$), the solution allows for an expansion in spherical harmonics. The leading term in this expansion corresponds to the quadrupole moment, which is given by

$$h_{ab}^{\text{quad}} = \frac{2}{r}\ddot{Q}_{ab}, \quad \text{where} \quad Q_{ab} = \int d^3x\, \rho(t, \mathbf{x}) \left(x_a x_b - \frac{1}{3} r^2 \delta_{ab} \right). \tag{2.17}$$

Here, $a, b = 1, 2, 3$ denote spatial indices, $\rho(t, \mathbf{x})$ is the mass density distribution varying in time, and the double dots indicate second time derivatives (a more detailed explanation for this result, including a comparison to electromagnetic radiation, can be found in [22]).

This result implies that GWs are produced by sources whose mass distributions exhibit a non-vanishing, time-dependent quadrupole moment. This is fundamentally different from electromagnetic radiation, which can also include dipole radiation due to the presence of both positive and negative charges. In contrast, gravitational radiation arises from the configuration and dynamics of masses alone, as mass is always positive and serves as the ”charge” of the gravitational interaction. Consequently, dipole gravitational radiation is absent.

Physically, the quadrupole moment characterizes how the distribution of mass changes around the system’s center of mass. Important consequences include the fact that perfectly spherical systems or those moving uniformly without internal dynamics do not emit GWs. This fact becomes particularly relevant when considering bubble nucleation during FOPTs. Although the initial expansion of an individual bubble is approximately spherical and thus does not source gravitational waves, subsequent interactions such as bubble collisions can break this symmetry. These processes can induce time-dependent quadrupole moments, leading to the generation of GWs, as will be discussed in more detail in chapter 3.

The formation of bubbles during FOPTs, as described in subsection 2.1.2, is a stochastic process, occurring simultaneously at different locations in the early universe. Each bubble acts as a gravitational wave source with varying amplitude and frequency. The superposition of these signals results in a SGWB. Detecting a background with features characteristic of FOPTs would provide evidence for such processes in the early universe. This motivates a more detailed examination of the SGWB in the following subsection (subsection 2.2.2).

2.2.2 The Stochastic Gravitational Wave Background

In this subsection, we introduce the SGWB, drawing on Refs. [19, 11].

Many physical processes in the early universe, such as FOPTs, involve numerous independent events that each emit gravitational radiation. When such emissions occur nearly simultaneously across causally disconnected regions, the resulting GW signal is a superposition of many incoherent sources. This results in a SGWB, whose properties are determined by statistical averages rather than individual deterministic signals.

To quantify the contribution of a SGWB to the total energy content of the universe, one introduces the dimensionless energy-density spectrum, $\Omega_{\text{GW}}(f)$. It describes how the gravitational wave energy density is distributed across different frequencies. This is defined relative to the critical energy density in natural units $\rho_c = \frac{3H_0^2}{8\pi}$ (H_0 is the Hubble rate today), required for a spatially flat universe, via:

$$\Omega_{\text{GW}}(f) \equiv \frac{1}{\rho_c} \frac{d\rho}{d \ln f}, \tag{2.18}$$

where $\frac{d\rho}{d \ln f}$ denotes the energy density in GWs per logarithmic frequency interval. The GW energy density itself can be computed from the effective stress-energy tensor of GWs. The spatially averaged energy density is:

$$\rho_{\text{GW}} = \frac{1}{32\pi} \left\langle \dot{h}_{ab} \dot{h}^{ab} \right\rangle, \tag{2.19}$$

where $\dot{h}_{ab}$ denotes the time derivative of the metric perturbation and the angle brackets indicate a spatial average. Using the spatial average is necessary, since the SGWB represents a random superposition of many independent sources, making only statistical descriptions meaningful.

In the TT gauge, the metric perturbation is expressed as a plane-wave expansion:

$$h_{ab}(t, \mathbf{x}) = \sum_{A=+,\times} \int_{-\infty}^{\infty} df \int_{S^2} d^2\Omega_{\hat{n}}\, h_A(f, \hat{n})\, e^{2\pi i f (t + \hat{n} \cdot \mathbf{x})}\, e_{ab}^A(\hat{n}). \tag{2.20}$$

The functions $h_A(f, \hat{n})$ are complex random fields, whose moments provide information about the statistical properties of the SGWB. $e_{ab}^A(\hat{n})$ are the polarization tensors defined perpendicular to the line of sight $\hat{n}$ to the GW source.

Assuming the background is statistically homogeneous, isotropic, unpolarized, and stationary, the quadratic expectation value of the Fourier modes are given by:

$$\langle h_A(f,\hat{n}) h^*_{A'}(f',\hat{n}') \rangle = \delta_{AA'} \delta(f-f') \delta^{(2)}(\hat{n},\hat{n}') \frac{1}{16\pi} S_h(f). \tag{2.21}$$

Here $S_h(f)$ is the one-sided power spectral density (PSD) of the GW signal.
Using this, the ensemble average of the squared time derivative of the metric perturbation evaluates to:

$$\langle \dot{h}_{ab} \dot{h}^{ab} \rangle = 8\pi^2 \int_0^\infty df\, f^2 S_h(f), \tag{2.22}$$

so that the differential energy density becomes:

$$\frac{d\rho_{\mathrm{GW}}}{d\ln f} = \frac{\pi}{4} f^3 S_h(f). \tag{2.23}$$

Finally, substituting this into the definition of $\Omega_{\mathrm{GW}}(f)$ gives:

$$\Omega_{\mathrm{GW}}(f) = \frac{2\pi^2}{3H_0^2} f^3 S_h(f). \tag{2.24}$$

The quantity $\Omega_{\mathrm{GW}}(f)$ is commonly used to describe the spectral shape of a SGWB and to compare theoretical models with observational bounds. For PTs, features such as the peak frequency and the spectral slopes, which are encoded in $\Omega_{\mathrm{GW}}(f)$, can be traced back to the physical parameters of the transition, such as its temperature, strength, and duration.

So far we have established the formalism needed to compute the SGWB spectrum. The precise spectral shape $S_h(f)$ (or equivalently $\Omega_{GW}(f)$) produced by certain processes, such as bubble collisions in a first-order phase transition, cannot be obtained analytically with sufficient accuracy and therefore requires numerical simulations. Such simulations are necessary to capture the full source dynamics, including e.g. non-linear effects. This step represents the transition from simplified theoretical modeling to quantitative predictions that can then be tested against observations.

2.2.3 Detection of a Stochastic Gravitational Wave Background with PTAs

In this subsection, we outline how PTAs can be used to detect a SGWB, following the presentation in [11]. PTAs monitor the arrival times of pulses from an array of millisecond pulsars, providing sensitivity in the nanohertz band. This regime is especially interesting, since astrophysical sources such as inspiralling supermassive black-hole binaries and cosmological mechanisms like first-order phase transitions are expected to generate a background in this range. Passing GWs perturb the spacetime metric along the photon trajectory from the pulsar to Earth, leading to small but measurable shifts in arrival times.

Working in the transverse-traceless gauge, the perturbed metric takes the form

$$ds^2 = -dt^2 + \big(\delta_{ab} + h_{ab}^{\mathrm{TT}}(t, \mathbf{x})\big)\, dx^a\, dx^b, \tag{2.25}$$

with $a, b = 1, 2, 3$. For a photon propagating along the x-axis towards the origin, the null condition $ds^2 = 0$ implies, to first order,

$$\frac{dx}{dt} \simeq -\Big(1 - \tfrac{1}{2} h_{xx}^{\mathrm{TT}}(t, \mathbf{x})\Big). \tag{2.26}$$

Integrating between emission t_{em} and observation t_{obs} yields

$$L \equiv x(t_{\text{em}}) - x(t_{\text{obs}}) = t_{\text{obs}} - t_{\text{em}} - \tfrac{1}{2} \int_{t_{\text{em}}}^{t_{\text{obs}}} dt'\, h_{xx}^{\mathrm{TT}}(t', \mathbf{x}(t')), \tag{2.27}$$

where L is the Earth–pulsar separation. Because h_{ab}^{TT} is small, the upper integration limit can be approximated as $t_{\text{em}} + L$, and the unperturbed photon path $\mathbf{x}(t) = (t_{\text{obs}} - t)\hat{p}$ is used.

For a general pulsar direction $\hat{p}$ one obtains

$$t_{\text{obs}} = t_{\text{em}} + L + \tfrac{1}{2}\hat{p}^a\hat{p}^b \int_{t_{\text{em}}}^{t_{\text{em}}+L} dt'\, h_{ab}^{\text{TT}}(t', (t_{\text{em}} + L - t')\hat{p})\,. \tag{2.28}$$

The arrival time of a subsequent pulse emitted one pulsar period P later can be treated analogously, so that their difference reads

$$t'_{\text{obs}} - t_{\text{obs}} = P + \Delta P, \tag{2.29}$$

with GW-induced deviation

$$\Delta P = \tfrac{1}{2}\hat{p}^a\hat{p}^b \int_{t_{\text{em}}}^{t_{\text{em}}+L} dt' \left[h_{ab}^{\text{TT}}(t' + P, \mathbf{x}_0(t')) - h_{ab}^{\text{TT}}(t', \mathbf{x}_0(t'))\right], \tag{2.30}$$

where $\mathbf{x}_0(t') = (t_{\text{em}} + L - t')\hat{p}$. As the GW period is much longer than P, expanding to first order gives

$$\frac{\Delta P}{P} = \frac{p^a p^b}{2} \int_{t_{\text{em}}}^{t_{\text{em}}+L} dt' \left[\frac{\partial}{\partial t'} h_{ab}^{\text{TT}}(t', \mathbf{x})\right]_{\mathbf{x}=\mathbf{x}_0(t')}. \tag{2.31}$$

This motivates defining the fractional frequency shift (redshift)

$$z(t) = \frac{\Delta P}{P}. \tag{2.32}$$

A plane GW in direction $\hat{\Omega}$ is modeled as

$$h_{ab}^{\text{TT}}(t', \mathbf{x}) = A_{ab}(\hat{\Omega}) \cos\!\big[\omega_{\text{GW}}(t' - \hat{\Omega}\cdot\mathbf{x})\big], \tag{2.33}$$

which leads to a redshift

$$z(t) = \tfrac{1}{2}\, \frac{\hat{p}^a\hat{p}^b}{1 + \hat{\Omega}\cdot\hat{p}} \Big[h_{ab}^{\text{TT}}(t, \mathbf{x}_e) - h_{ab}^{\text{TT}}(t - L, \mathbf{x}_p)\Big], \tag{2.34}$$

where $\mathbf{x}_e$ and $\mathbf{x}_p = L\hat{p}$ are the Earth and pulsar positions. The two contributions are referred to as the *Earth term*, common to all pulsars, and the *pulsar term*, which depends on each pulsar’s distance and orientation.

The cumulative effect is captured by the timing residual

$$r(t) = \int_0^t z(t')\, dt', \tag{2.35}$$

which is the central observable in PTA analyses.

In the frequency domain, the redshift induced by a GW in direction $\hat{\Omega}$ reads

$$\tilde{z}(f, \hat{\Omega}) = \left[e^{-2\pi i f L(1+\hat{\Omega}\cdot\hat{p})} - 1\right] \sum_{A=+,\times} h_A(f, \hat{\Omega})\, F^A(\hat{\Omega}), \tag{2.36}$$

where the antenna response is

$$F^A(\hat{\Omega}) = \tfrac{1}{2}\, \frac{\hat{p}^a \hat{p}^b}{1 + \hat{\Omega}\cdot\hat{p}}\, e^A_{ab}(\hat{\Omega}). \tag{2.37}$$

Detecting a SGWB relies on cross-correlating the redshift signals from different pulsars, which removes uncorrelated noise and isolates the common GW contribution.

Averaging over all GW directions and assuming Gaussianity, stationarity, isotropy, and equal polarization content yields the ensemble-averaged cross-power spectral density

$$\left\langle \tilde{z}_i(f) \tilde{z}_j^*(f') \right\rangle = \tfrac{1}{2}\, \delta(f - f')\, S_s(f)_{ij}, \tag{2.38}$$

with

$$S_s(f)_{ij} = \tfrac{1}{2} S_h(f) \int_{S^2} \frac{d^2\hat{\Omega}}{4\pi}\, \kappa_{ij}(f, \hat{\Omega}) \sum_A F_i^A(\hat{\Omega}) F_j^A(\hat{\Omega}), \tag{2.39}$$

where $S_h(f)$ is the one-sided strain power spectral density and

$$\kappa_{ij}(f, \hat{\Omega}) = \left[e^{-2\pi i f L_i(1+\hat{\Omega}\cdot\hat{p}_i)} - 1\right]\left[e^{+2\pi i f L_j(1+\hat{\Omega}\cdot\hat{p}_j)} - 1\right]. \tag{2.40}$$

Since for nanohertz frequencies $f L_i \gg 1$, the exponential factors average out unless $i = j$, giving

$$\kappa_{ij}(f, \hat{\Omega}) \;\to\; \begin{cases} 2, & i = j, \\ 1, & i \neq j. \end{cases} \tag{2.41}$$

Hence $S_s(f)_{ij}$ becomes frequency independent up to $S_h(f)$, and one defines the unnormalized overlap reduction function

$$\tilde{\Gamma}_{ij} = \int_{S^2} \frac{d^2\hat{\Omega}}{4\pi} \sum_A F_i^A(\hat{\Omega}) F_j^A(\hat{\Omega}), \tag{2.42}$$

so that

$$S_s(f)_{ij} = \tfrac{1}{2} S_h(f) \tilde{\Gamma}_{ij}. \tag{2.43}$$

Hellings & Downs first derived an unnormalized version [23]; here we quote the normalized form commonly used in PTA analyses:

$$\Gamma_{ij} = \tfrac{3}{2} x_{ij} \ln x_{ij} - \tfrac{1}{4} x_{ij} + \tfrac{1}{2} + \tfrac{1}{2}\delta_{ij}, \tag{2.44}$$

with $x_{ij} = (1 - \cos\theta_{ij})/2$, so Γ_{ij} depends only on the angular separation θ_{ij}. This angular correlation pattern, shown in Figure 2.5, is the characteristic signature of an isotropic SGWB in GR, which PTAs are designed to detect.

The next chapter focuses on the generation of SGWBs in FOPTs.

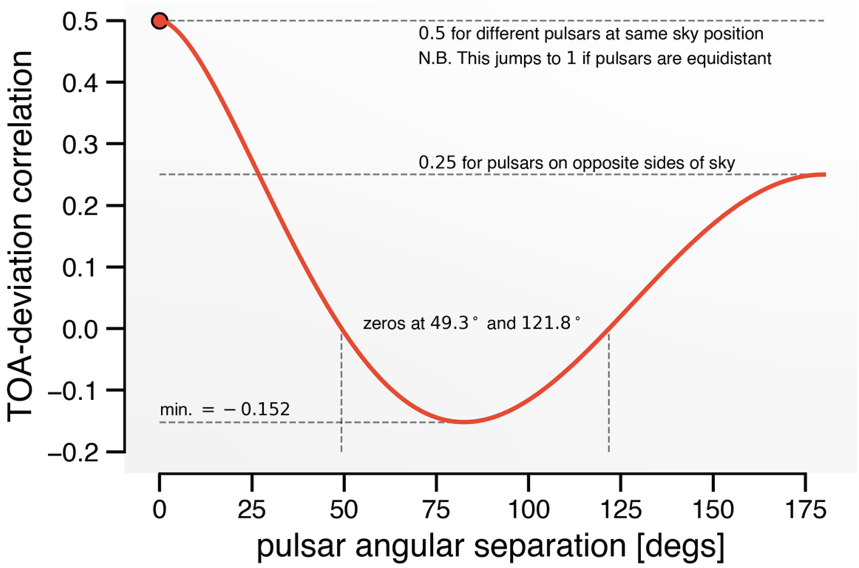

Figure 2.5: Hellings & Downs curve: normalized correlation of pulsar timing residuals as a function of angular separation, expected for an isotropic SGWB in GR (taken from [11]).

Gravitational Waves from a First Order Phase Transition

3

3.1 Sources for Gravitational Waves

As we have seen in chapter 2, a cosmological FOPT proceeds through nucleation of bubbles of the new vacuum; the growth and interactions of these bubbles are the physical processes that can generate GWs. Perfectly spherical, isolated objects do not emit gravitational radiation because their energy distribution lacks higher multipole moments. Only when spherical symmetry is broken, for instance by overlapping bubbles or by disturbances in the surrounding plasma, does a nonzero quadrupole moment develop and GWs are produced [12].

If the particles in the primordial plasma couple sufficiently to the field driving the transition, a large fraction of the latent heat is transferred into the medium. This energy deposition produces heated, expanding shells of plasma around the scalar-field bubble walls. These shells carry kinetic and thermal energy and can interact hydrodynamically when different bubbles grow and meet. The plasma dynamics therefore plays a central role in the GW production for transitions in this regime.

In the opposite limit, when the coupling between the plasma and the transition field is weak, most of the released energy is converted into the motion of the scalar-field bubble walls. The walls may then accelerate to highly relativistic velocities and carry a significant portion of the transition energy themselves. Collisions of such energetic walls also source GWs, but the subsequent evolution of the system differs from the plasma-dominated case.

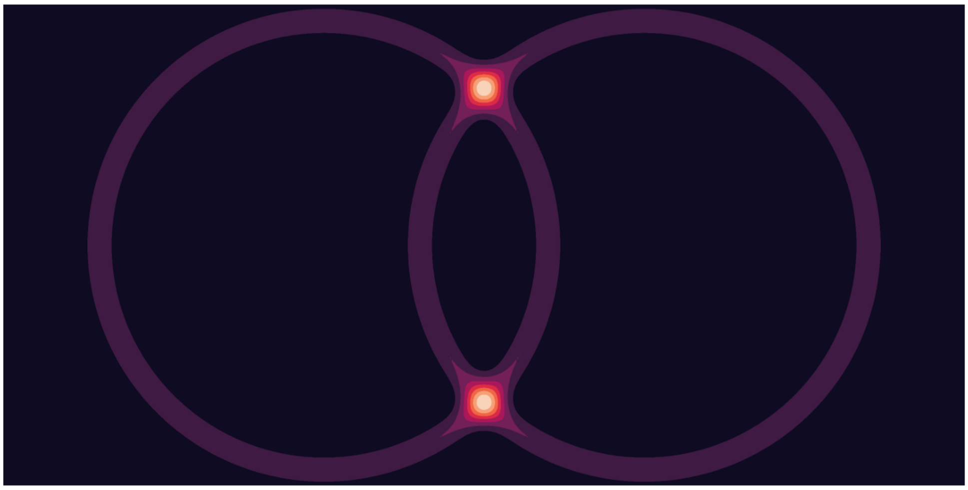

Figure 3.1: Illustration of the squared fluid four-velocity $U^\mu U_\mu$ for two overlapping plasma shells during a FOPT (figure taken from Ref. [12]). Bright regions mark local overdensities of the fluid velocity where shells overlap; these inhomogeneities break spherical symmetry and give rise to a non-vanishing quadrupole moment.

Both the bubble walls and the perturbed plasma source the gravitational field through the stress-energy tensor. For the plasma component one commonly writes

$$T^{\mu\nu}_{(f)} = (e + p)\, U^\mu U^\nu, \tag{3.1}$$

where e and p denote the plasma energy density and pressure, and U^μ the fluid four-velocity. The four-velocity appears quadratically, so any region where shells overlap produces local variations in $T^{\mu\nu}_{(f)}$ that break spherical symmetry and produce GWs (a nonzero quadrupole). In practice, three mechanisms are usually distinguished as the dominant GW sources in a FOPT:

1. **Direct scalar-field (wall) collisions:** When bubble walls meet and the scalar field relaxes to the new vacuum, the resulting dynamics can radiate gravitationally.

2. **Sound-wave contribution:** After the walls have passed, heated regions propagate as shells of sound waves. Overlaps of these acoustic shells are a long-lived and often the dominant source of GWs in many models.

3. **Nonlinear effects:** For sufficiently strong transitions nonlinear hydrodynamic effects (e.g. turbulence) can develop and amplify the GW signal.

Following these considerations, the SGWB arises from the combined effect of these contributions. The next subsection provides more quantitative estimates of the resulting energy-density spectrum $\Omega_{\rm GW}(f)$.

3.2 Modelling the Gravitational Wave Spectrum

This section is based on [24]. It summarises how simple dimensional arguments (following [25]), supplemented by numerical fits, lead to an approximate form for the SGWB from an FOPT.

We assume that the characteristic quantities controlling the GW production are Newton's constant G, the amount of vacuum energy available to source GWs (usually written as $\kappa\rho_V$, where κ is the efficiency factor), the typical bubble-wall velocity v_w, and the timescale of the transition β^{-1} (typically the duration of the transition, related to the bubble nucleation rate). If no other mass or time scales enter, dimensional analysis fixes the scaling of the total GW energy. It follows:

$$E_{\rm GW} \sim G\, v_w^3\, \kappa^2\, \rho_V^2\, \beta^{-5}$$

The total vacuum energy liberated scales as

$$E_V \sim \rho_V\, v_w^3\, \beta^{-3}.$$

Taking the ratio gives the fraction of the released vacuum energy converted into gravitational radiation,

$$r \equiv \frac{E_{\rm GW}}{E_V} \sim \kappa^2 \left(\frac{\beta}{\sqrt{G\rho_V}} \right)^{-2}.$$

Using the Friedmann relation $H_* \sim \sqrt{G\rho_{\text{tot}}}$ and the strength parameter $\alpha \equiv \rho_V/\rho_R$ (so that $\rho_V/\rho_{\text{tot}} = \alpha/(1+\alpha)$), the last expression can be rewritten as

$$r \sim \kappa^2 \frac{\alpha}{1+\alpha} \left(\frac{\beta}{H_*}\right)^{-2}.$$

Dividing by the total energy density at the time of production, the GW energy density fraction scales as

$$\frac{\rho_{\text{GW}}}{\rho_{\text{tot}}} \sim \kappa^2 \left(\frac{\alpha}{1+\alpha}\right)^2 \left(\frac{\beta}{H_*}\right)^{-2}.$$

Introducing a dimensionless spectral shape function g, whose argument can be taken as f/β, we therefore obtain the parametrised spectrum at production

$$\frac{1}{\rho_{\text{tot}}} \frac{d\rho_{\text{GW}}}{d\ln f} \simeq \kappa^2 \left(\frac{\alpha}{1+\alpha}\right)^2 \left(\frac{\beta}{H_*}\right)^{-2} g(f/\beta).$$

Since β^{-1} is the only timescale in this simplified argument, the peak of g is expected near $f \sim \beta$.

Simulations and causality arguments further constrain the spectral form. At low frequencies the spectrum rises as $\propto f^3$ (a consequence of causality), while at high frequencies it must fall off sufficiently fast so that the total GW energy remains finite. A broken power law (BPL) provides a simple template that reproduces these features.

After redshifting the spectrum to the present day, a general proportional template for the observable signal is

$$\underbrace{h^2\Omega_{\mathrm{GW}}(f)}_{\text{Observable}} \propto \underbrace{1.64\times 10^{-5}\left(\frac{100}{g_{\mathrm{eff},*}}\right)^{1/3}}_{\text{Redshift}} \underbrace{\kappa^2\left(\frac{\alpha}{1+\alpha}\right)^2\left(\frac{\beta}{H_*}\right)^{-2}}_{\text{Scaling}} \underbrace{\mathcal{S}(f;\, f_{\mathrm{peak}},\dots)}_{\text{Shape}}, \tag{3.2}$$

where:

- ▷ Redshift denotes the factor that maps the energy density at production to today's one (dependent on the effective degrees of freedom $g_{\mathrm{eff},*}$). More on that in subsection 3.2.1.
- ▷ Scaling encodes the dimensional scalings with the thermal parameters $\{\alpha, \beta/H_*, \kappa, v_w\}$ that determine the overall amplitude.
- ▷ Shape is a source-dependent dimensionless function (often fitted by a single or double-broken power law (DBPL)), which fixes the spectral profile and the locations of one or more characteristic frequencies f_{peak} relevant for the source.

The SGWB spectrum is always reported in terms of $h^2\Omega_{GW}$, which accounts for the uncertainty in the Hubble parameter H_0 through the dimensionless quantity h ($H_0 = 100\,h\,\mathrm{k}m/s/Mpc$).
It is important to note that, instead of characterising the observable spectrum through thermodynamic parameters (which determine the *redshift* and the overall *scaling*), we can equivalently describe the spectrum using purely geometric parameters. For instance, when the shape function is modelled as a single broken power law (SBPL), a compact geometric parameterisation θ_{geom} may consist of the amplitude at the spectral peak and the peak frequency ($\theta_{geom} = \{\Omega_{\mathrm{p}},\, f_{\mathrm{p}}\}$) together with the relevant spectral slopes.

This geometric parameterisation is convenient for phenomenological fits and for direct comparison with detector sensitivity curves, because it parametrises the observable features of the spectrum. However, it does not provide direct information about the underlying thermodynamic parameters of the phase transition, such as the transition temperature T_* or the strength parameter α.

For these reasons, the analysis presented in chapter 5 reports spectra in both forms: (i) using thermodynamic parameters and the scaling/redshift template, and (ii) using the corresponding geometric parameters.

3.2.1 Redshift

The observed spectrum today is obtained from the production-frame spectrum by accounting for the cosmic expansion. To start, the Friedmann equations, derived from Einstein's equations under the assumptions of homogeneity and isotropy with a flat Friedmann–Lemaître–Robertson–Walker (FLRW) metric are introduced,

$$ds^2 = -dt^2 + a^2(t)\,\delta_{ij}\,dx^i dx^j, \tag{3.3}$$

where $a(t)$ is the scale factor. For a perfect fluid with total energy density ρ and pressure p, Einstein's equations reduce to

$$H^2 = \left(\frac{\dot{a}}{a}\right)^2 = \frac{8\pi G}{3}\,\rho, \tag{3.4}$$

$$\frac{\ddot{a}}{a} = -\frac{4\pi G}{3}\,(\rho + 3p), \tag{3.5}$$

where H is the Hubble parameter. During radiation domination, $p = \rho/3$, and the energy density decreases with the expansion of the universe as $\rho \sim a^{-4}$. Assuming entropy conservation, the scale factor is inversely proportional to the temperature, $a \sim T^{-1}$ (later shown in Equation 3.9), which leads to

$$\rho_{\text{rad}}(T) = \frac{\pi^2}{30}\,g_{\text{eff}}(T)\,T^4, \tag{3.6}$$

with $g_{\text{eff}}(T)$ the effective number of relativistic degrees of freedom contributing to the energy density.

Considering a characteristic source frequency f_* at production, the observed frequency today is

$$f_0 \;=\; \frac{a_*}{a_0}\, f_*. \tag{3.7}$$

The ratio of scale factors follows from entropy conservation. The entropy density of a relativistic plasma is

$$s(T) \;=\; \frac{2\pi^2}{45}\, g_s(T)\, T^3, \tag{3.8}$$

with $g_s(T)$ the effective number of entropic degrees of freedom. Adiabatic expansion implies $s\, a^3 = \mathrm{const}$, hence

$$\frac{a_*}{a_0} \;=\; \left(\frac{g_{s,0}}{g_{s,*}}\right)^{1/3} \frac{T_0}{T_*}, \tag{3.9}$$

where $T_0 \simeq 2.73$ K is today's photon temperature and $g_{s,0} \simeq 3.91$. The temperature at production T_*, is typically taken to be the temperature at the end of the PT in the specific case of FOPTs. To proceed, the Friedmann equation during radiation domination is combined with Equation 3.6, yielding

$$H_*^2 \;=\; \frac{8\pi^3 G}{90}\, g_{\mathrm{eff},*}\, T_*^4. \tag{3.10}$$

This relation links the Hubble scale to the plasma temperature and leads to a mild g_{eff}–dependence of the redshifted frequency.[1] Inserting Equation 3.9 into Equation 3.7 and using Equation 3.10 leads to the practical expression

$$f_0 \;\simeq\; \underbrace{1.65 \times 10^{-5}\,\mathrm{Hz} \left(\frac{g_{\mathrm{eff},*}}{100}\right)^{1/6} \left(\frac{T_*}{100\,\mathrm{GeV}}\right)}_{H_{*,0}} \left(\frac{f_*}{H_*}\right). \tag{3.11}$$

---

[1] At high temperatures we typically assume $g_{\mathrm{eff},*} \simeq g_{s,*}$, since all relativistic degrees of freedom are in thermal equilibrium. At late times, however, we must distinguish between the entropic degrees of freedom g_s (relevant for entropy conservation) and the energy degrees of freedom g_{eff} (relevant for ρ_{rad}). Today, for instance, $g_{s,0} \simeq 3.91$ while $g_{\mathrm{eff},0} \simeq 3.36$.

$H_{*,0}$ is the Hubble rate at the time of GW production, redshifted to today. If the characteristic source frequency is set by the inverse transition timescale β (so that $f_*/H_* \sim \beta/H_*$) the following equation is obtained:

$$f_0 \;\simeq\; 1.65 \times 10^{-5}\,\mathrm{Hz}\,\left(\frac{g_{\mathrm{eff},*}}{100}\right)^{1/6}\left(\frac{T_*}{100\,\mathrm{GeV}}\right)\left(\frac{\beta}{H_*}\right). \tag{3.12}$$

Due to the GW energy density redshifting as $\rho_{\mathrm{GW}} \propto a^{-4}$ and the critical density today being $\rho_{c,0} = 3H_0^2/(8\pi G)$, the fractional GW density transforms as

$$\Omega_{\mathrm{GW},0} \;=\; \left(\frac{a_*}{a_0}\right)^4\left(\frac{H_*}{H_0}\right)^2\Omega_{\mathrm{GW},*}. \tag{3.13}$$

Using Equation 3.9 and Equation 3.10 and inserting the standard values for the present-day cosmological parameters, we arrive at the result

$$\Omega_{\mathrm{GW},0}\,h^2 \;\simeq\; \underbrace{1.64 \times 10^{-5}\left(\frac{100}{g_{\mathrm{eff},*}}\right)^{1/3}}_{F_{\mathrm{GW},0}}\,h^2\,\Omega_{\mathrm{GW},*}. \tag{3.14}$$

Here $F_{\mathrm{GW},0}$ is the redshift factor for the fractional energy density. Equation 3.12 and Equation 3.14 together summarise how a primordial GW signal is mapped to today's observable frequency and amplitude.

Summary of PTA Analysis

4

In order to connect theoretical models of new-physics signals to PTA data, the Python-based framework `PTArcade` [26] has been developed as a wrapper around the existing PTA analysis tools `enterprise` [27, 28] and `ceffyl` [29]. `PTArcade` allows users to specify new-physics motivated signals in two ways: either through the gravitational-wave energy density spectrum

$$\Omega_{\mathrm{GW}}(f;\,\vec{\theta}), \tag{4.1}$$

for stochastic backgrounds, or via the time-domain strain signal

$$h(t;\,\vec{\theta}), \tag{4.2}$$

for deterministic signals. Here, $\vec{\theta}$ denotes the set of model parameters characterizing the signal.

In this work, the first approach is used, i.e. directly implementing models for the GW energy density spectrum $\Omega_{\mathrm{GW}}(f)$ that arise from cosmological FOPTs. An example model file implementation in `PTArcade` is provided in subsection 4.2.4 at the end of this chapter. At this point it is important to note that the SMBHB foreground also influences the measured GWB. This will be further explained in the next section. The posterior probability distributions and parameter constraints are then obtained within a Bayesian framework, as discussed afterwards.

4.1 Astrophysical Background

SMBHBs are an important expected astrophysical source of nanohertz GWs. Such binaries form in the aftermath of galaxy mergers and gradually inspiral due to gravitational radiation. Their collective signal contributes to a stochastic background that can be approximated by a power law of the form [26]

$$h^2\Omega_{\mathrm{GW}}^{\mathrm{BHB}}(f) \;=\; \frac{2\pi^2}{3H_0^2}\, A_{\mathrm{BHB}}^2 \left(\frac{f}{\mathrm{yr}^{-1}}\right)^{5-\gamma_{\mathrm{BHB}}} \mathrm{yr}^{-2}. \tag{4.3}$$

Both the amplitude A_{BHB} and the spectral index γ_{BHB} are free parameters that need to be determined from observational data.

When the flag `smbhb=True` is set (in `PTArcade`), Equation 4.3 is automatically added to any user-specified cosmological signal. Each FOPT induced GWB model is implemented both as the sole source of the GWB and together with the SMBHB foreground, in order to explore the ranges of thermodynamic and geometric parameters that would be consistent with the observed GWB, under the assumption that the model is valid.

4.2 Statistical Tools and Implementation

This section summarises the statistical tools used in this work. It follows their implementation in `PTArcade`. The PTA likelihood is stated and how user-provided spectra are mapped into the likelihood inputs. Then a concise introduction to Bayesian inference and to Markov chain Monte Carlo sampling, using the Metropolis–Hastings formalism, is given.

4.2.1 PTA Likelihood and Spectral Relation

PTA analyses operate on timing residuals, $\boldsymbol{\delta t}$, i.e. the difference between observed pulse times of arrival and predictions from the pulsar timing model. Residuals are modelled as

$$\boldsymbol{\delta t} = \boldsymbol{n} + F\boldsymbol{a} + M\boldsymbol{\epsilon}, \tag{4.4}$$

where $\boldsymbol{n}$ denotes white noise, F is a Fourier design matrix (sine–cosine pairs at frequencies i/T_{obs}), $\boldsymbol{a}$ are Fourier coefficients for time-correlated processes (intrinsic red noise and GWB signals), M is the timing-model design matrix, and $\boldsymbol{\epsilon}$ are small timing-model offsets.

The Fourier coefficients are Gaussian random variables with covariance

$$\langle a_{a,i} a_{b,j} \rangle = \delta_{ij} \left(\Gamma_{ab} \, \Phi_i + \delta_{ab} \, \phi_{a,i} \right), \tag{4.5}$$

where a, b index the pulsars, i, j the frequency harmonics, Γ_{ab} is the overlap reduction function (Hellings–Downs for an isotropic GR background as explained in subsection 2.2.3), Φ_i encodes the common spectral power in bin i, and $\phi_{a,i}$ is pulsar-specific red noise.

The coefficients Φ_i are directly related to the GW energy density spectrum via

$$h^2 \Omega_{\text{GW}}(f) \;=\; \frac{8\pi^4}{H_0^2/h^2} \, f^5 \, \frac{\Phi(f)}{\Delta f}, \tag{4.6}$$

with $\Delta f \;=\; 1/T_{\text{obs}}$ being the width of the N_f frequency bins, where T_{obs} is the total observation time. Via this relationship, any user-defined model $\Omega_{\text{GW}}(f)$ is automatically converted by `PTArcade` into the covariance of the Fourier coefficients entering Equation 4.5.

The full likelihood for the timing residuals, after marginalising over $\boldsymbol{a}$ and $\boldsymbol{\epsilon}$, is:

$$p(\boldsymbol{\delta t} \mid \boldsymbol{\theta}) \;=\; \frac{\exp\big(-\tfrac{1}{2} \boldsymbol{\delta t}^T C^{-1} \boldsymbol{\delta t} \big)}{\sqrt{\det(2\pi C)}}, \tag{4.7}$$

with $C = N + TBT^T$, N the white-noise covariance, $T = [M, F]$, $\boldsymbol{\theta}$ the parameters describing the user-specified signal and $B = \text{diag}(\infty, \varphi)$. This form corresponds to the residual-level likelihood used by `enterprise`.

For testing purposes, the `ceffyl` likelihood was used, which approximates the per-frequency power spectrum and neglects inter-frequency correlations, allowing for faster, but less precise computations. The main results presented here rely on the full `enterprise` likelihood.

4.2.2 Bayesian Inference

All analyses in `PTArcade` rely on Bayesian inference in order to extract information on the parameters of a user-specified signal model from the pulsar timing residuals. Given the likelihood $p(\boldsymbol{\delta t} \mid \boldsymbol{\theta})$ and a prior probability distribution $p(\boldsymbol{\theta})$, Bayes' theorem gives the posterior probability distribution

$$p(\boldsymbol{\theta} \mid \boldsymbol{\delta t}) = \frac{p(\boldsymbol{\delta t} \mid \boldsymbol{\theta})\, p(\boldsymbol{\theta})}{\int p(\boldsymbol{\delta t} \mid \boldsymbol{\theta})\, p(\boldsymbol{\theta})\, \mathrm{d}\boldsymbol{\theta}}. \tag{4.8}$$

The denominator is the evidence. The likelihood quantifies how well a given set of model parameters $\boldsymbol{\theta}$ explains the observed data and the prior encodes any knowledge or assumptions about the parameters before considering the data. The main interest here lies in the posterior distribution, because it encodes the probability distribution of the model parameters (including those of the gravitational-wave signal) given the observed PTA data.

Depending on the chosen mode, `PTArcade` evaluates the likelihood either using the full PTA likelihood implemented in `enterprise` (Equation 4.7), or using the fast approximation of `ceffyl`.

In practice, the integrals appearing in Bayes' theorem are too computationally expensive to be solved analytically due to the high dimensionality of the parameter space. Instead, posterior sampling is carried out numerically using stochastic techniques. In particular, `PTArcade` employs the Markov Chain Monte Carlo (MCMC) tools, which are briefly explained next.

4.2.3 MCMC Sampling

This subsection is based on [11]. When the posterior is high-dimensional and cannot be integrated analytically, Markov chain Monte Carlo (MCMC) methods provide a practical approach. The idea is to construct a Markov chain whose stationary distribution equals the target posterior $p(\boldsymbol{\theta} \mid \boldsymbol{\delta t})$. One often uses the Metropolis–Hastings algorithm, where at each step a new point $\boldsymbol{\theta}'$ is proposed from a proposal distribution $q(\boldsymbol{\theta}' \mid \boldsymbol{\theta})$ and accepted with probability

$$\alpha = \min\left(1,\ \frac{p(\boldsymbol{\theta}')\, p(\boldsymbol{\delta t} \mid \boldsymbol{\theta}')}{p(\boldsymbol{\theta})\, p(\boldsymbol{\delta t} \mid \boldsymbol{\theta})} \times \frac{q(\boldsymbol{\theta} \,|\, \boldsymbol{\theta}')}{q(\boldsymbol{\theta}' \,|\, \boldsymbol{\theta})}\right). \tag{4.9}$$

If the proposal is accepted the chain moves to $\boldsymbol{\theta}'$, otherwise it remains at $\boldsymbol{\theta}$. After an initial burn-in phase, the chain produces samples that are distributed according to the posterior. They can then be used to estimate parameter distributions and uncertainties.

In summary, `PTArcade` automates: (i) the mapping of model spectra $\Omega_{\rm GW}(f)$ into the frequency-bin power coefficients Φ_i, which enter the covariance of the Fourier coefficients in the PTA likelihood; (ii) the construction of either the full likelihood provided by `enterprise` or the `ceffyl` likelihood and (iii) the Bayesian sampling of posteriors via MCMC.

In the next subsection, we provide and discuss an example implementation of a model file in `PTArcade`.

4.2.4 Example PTArcade Model File

In this subsection we show an example model file, which, together with a configuration file, provides the input to `PTArcade`. The configuration file is a Python script used to adjust different run parameters (for example the execution mode, e.g. `enterprise` or `ceffyl`).

The model file displayed in Listing 4.1 implements a case of a FOPT where the SGWB is dominated by the contribution of bubble collisions. The physical interpretation and results of this specific model are discussed in chapter 5. The structure of a `PTArcade` model file is generally the same across different models: First, the model parameters and their priors are declared. Then a shape function and a spectrum function specific to the model are implemented. In the example file the shape function is a BPL and the spectral function follows the template introduced in Equation 3.2.

Listing 4.1: Example Python model file for a SGWB by bubble collisions.

```
import numpy as np
from ptarcade.models_utils import prior
from ptarcade.models_utils import g_rho, g_s

name="bubble_collisions"

smbhb = False #excluding signal of SMBHBs

#defining set of parameters and their correspoding priors
parameters = {
            'log_T_star': prior("Uniform", -4, 4),
            'log_K_tilde': prior("Uniform", -5, 0),
            'log_H_star_R_star': prior("Uniform", -3, -0),
            'a_1': prior("Uniform", 0.2, 2.2),
            'n_1': prior("Uniform", 1.4, 3.4),
            'n_2': prior("Uniform", -3.4, -1.4)
            }


def S_p(x,n_1,n_2,a_1): #Spectral shape function
    return ((n_1 - n_2)**((n_1-n_2)/a_1)
            * 1/(-n_2 * x**(-n_1*a_1/(n_1-n_2)) + n_1
            * x**(-n_2*a_1/(n_1-n_2)))**((n_1-n_2)/(a_1)))


#GW spectrum for bubble collisions
def spectrum(f,log_T_star,log_K_tilde,log_H_star_R_star,a_1,n_1,n_2):

    #Temperature at PT
    T = 10**log_T_star
```

```
    #Hubble rate times mean bubble size
    H = 10**log_H_star_R_star
    #Fractional energy density of GW source
    K = 10**log_K_tilde

    v_w = 1 #Bubble-wall velocity
    A_str = 0.05 #Numerical prefactor from simulations

    #Frequency redshift
    H_star_0 = 1.65*10**(-5)*(g_rho(T)/100)**(1/6)*(T/100)

    #Amlitude redshift
    F_GW0 = 1.64*10**(-5)*(100/g_rho(T))**(1/3)

    #Peak amplitude
    A_p = F_GW0*A_str*K**2*(H/((8*np.pi)**(1/3)*v_w))**2

    #Peak frequency
    f_p = H_star_0*0.11*1/(H/((8*np.pi)**(1/3)*v_w))

    return A_p * S_p(f/f_p,n_1,n_2,a_1)
```

Many parameters are specified and sampled in logarithmic form (e.g. `log_T_star`, `log_K_tilde`). When a prior in the model file is written as `prior("Uniform", a, b)` for a parameter named `log_X`, this denotes a uniform prior on $\log_{10} X$ over the interval $[a, b]$:

$$p(\log_{10} X) = \begin{cases} \frac{1}{b-a} & \text{for } \log_{10} X \in [a, b], \\ 0 & \text{otherwise.} \end{cases} \tag{4.10}$$

Equivalently, the implied prior on the linear quantity X is

$$p(X) \propto \frac{1}{X}, \quad X \in [10^a, 10^b]. \tag{4.11}$$

This choice is mainly motivated by practical considerations. A log-uniform prior assigns equal prior weight per order of magnitude and therefore samples effectively across many orders of magnitude. This is often appropriate for parameters whose values span several orders of magnitude. Finally, the model file can include a boolean flag to add a SMBHB template to the total spectrum.

Results

5

This results section follows the approach of Ref. [13]. In this chapter the different templates for a GW spectrum from FOPTs, as presented by the LISA collaboration, are introduced. The templates were fit to the NANOGrav 15-year dataset [14]. Specifically, each template is expressed in terms of geometric and thermodynamic parameters. For each parameterization, we fit the model both alone and in combination with the additional SMBHB foreground to the data. The results of these analyses are shown below. The parameters used to describe the different templates are the same as those introduced in chapter 3, with the only exception that H_*R_*, the average bubble separation R_* in units of the Hubble radius at percolation, is used instead of the inverse duration of the transition $\frac{\beta}{H_*}$. These quantities are directly related via

$$H_*R_* = (8\pi)^{1/3}\,\max(v_w, c_s)\,\frac{H_*}{\beta}\,, \tag{5.1}$$

where c_s is the speed of sound. Any additional thermodynamic or geometric parameter appearing in a model will be explained in the relevant section.

5.1 Bubble Collisions and Highly Relativistic Fluid Shells

The SGWB signal from bubble collisions (and similarly from highly relativistic fluid shells) is modeled by a single broken power law (SBPL), as adopted in the LISA collaboration studies [1]. The SBPL is used for very strong FOPTs, characterized by

---

[1] For details on the numerical modeling of bubble collisions and fluid shells, see e.g. [30, 31].

a large vacuum energy compared to the radiation background ($\alpha \gg 1$). In this regime, the bubble walls accelerate rapidly and can be approximated as moving at the speed of light ($v_w \simeq 1$). In its geometric form, the template is expressed as

$$\Omega_{\text{SBPL}}(f;\,\Omega_b, f_b, n_1, n_2, a_1) = \Omega_b \left(\frac{f}{f_b}\right)^{n_1} \left(\frac{1}{2} + \frac{1}{2}\left(\frac{f}{f_b}\right)^{a_1}\right)^{\frac{n_2-n_1}{a_1}}\,, \tag{5.2}$$

where the parameters $\{\Omega_b, f_b\}$ represent the free *geometric* degrees of freedom and n_1, n_2, a_1 describe spectral parameters: the low- and high-frequency slopes (n_1, n_2), as well as the width of the transition a_1. While the spectral parameters are fixed in the LISA paper, for this analysis they are also treated as free parameters (more on that in subsection 5.1.1). The amplitude is normalized such that $\Omega_{\text{SBPL}}(f_b) = \Omega_b$. In general, the scale f_b does not coincide with the spectral maximum f_p. The latter is located at

$$f_p = f_b \left(-\frac{n_1}{n_2}\right)^{1/a_1}\,, \tag{5.3}$$

and the amplitude at the peak Ω_p is related to Ω_b

$$\Omega_p = \Omega_b \left[\frac{1}{2}\left(-\frac{n_2}{n_1}\right)^{\frac{n_1}{n_1-n_2}} + \frac{1}{2}\left(-\frac{n_1}{n_2}\right)^{\frac{-n_2}{n_1-n_2}}\right]$$

and Ω_p is related to the thermodynamic parameters via:

$$h^2\Omega_p = h^2 F_{\text{GW},0}\, A_{\text{str}}\, \tilde{K}^2 \left(\frac{H_* R_*}{(8\pi)^{1/3}}\right)^2\,, \tag{5.4}$$

$$f_p = 0.11\, H_{*,0}\, \frac{(8\pi)^{1/3}}{H_* R_*}\,, \tag{5.5}$$

where $\tilde{K} \equiv \alpha/(1+\alpha)$ denotes the fractional energy density of the source and A_{str} is a numerical efficiency factor from simulations (for the considered model $A_{\text{str}} \simeq 0.05$). In this specific case, apart from the factor A_{str}, the expression in Equation 5.4 happens to share the same exact form as the general template introduced in Equation 3.2.

The relations explicitly show how the thermodynamic parameters determine the observable peak quantities (f_p, Ω_p). In terms of these quantities, the SGWB spectrum is expressed as follows:

$$\Omega^{\mathrm{GW}}_{\mathrm{SBPL}}(f, \vec{\theta}_{\mathrm{cosmo}}) = \Omega_p \frac{(n_1 - n_2)^{\frac{n_1-n_2}{a_1}}}{\left[-n_2 \left(\frac{f}{f_p}\right)^{\frac{-n_1 a_1}{n_1-n_2}} + n_1 \left(\frac{f}{f_p}\right)^{\frac{-n_2 a_1}{n_1-n_2}}\right]^{\frac{n_1-n_2}{a_1}}} . \tag{5.6}$$

5.1.1 Priors

In contrast to the reference assumptions, the priors in this analysis were not fixed to the values studied by the LISA collaboration.

For the analysis of the bubble collision template, the prior distributions of the model parameters were adapted to the frequency range relevant for PTA observations. In particular, the geometric parameter f_b was shifted from the LISA band ($f \sim 10^{-4} - 10^{-1}\,\mathrm{Hz}$) to the nanohertz range. This range is typical for PTA data ($f \sim 10^{-9} - 10^{-7}\,\mathrm{Hz}$). Correspondingly, the temperature at the end of the phase transition T_* was adjusted, as the present-day peak frequency is related to T_* through the redshift factor (see Equation 3.9). The amplitudes Ω_b and the fractional energy density parameter $\tilde{K}$ were kept fixed relative to the values reported in the LISA analysis, since these parameters do not directly depend on the frequency range.

For the thermodynamic timescale, the inverse duration β/H_* was replaced by the average bubble separation H_*R_* in comparison to the LISA analysis. The prior on H_*R_* is physically bounded, excluding bubbles that would exceed the Hubble radius and thus not be in causal contact (meaning $H_*R_* < 1$).

Finally, the spectral shape parameters n_1, n_2, and a_1 were taken from the LISA analysis, but their priors were extended by ± 1 to allow for additional flexibility in the spectral form. This led to the choice of priors seen in Table 5.1:

5.1.2 Posterior Distributions and Parameter Constraints

Posterior distributions for both the geometric parameters $\{\log_{10} \Omega_b, \log_{10} f_b\}$ and the corresponding thermodynamic parameters are presented below. The numerical

Table 5.1: Prior ranges for the thermodynamic, geometric and spectral parameters of the bubble collision template.

Parameter	Prior (Uniform)
Thermodynamic parameters	
$\log_{10} T_*$	$[-4,\ 4]$
$\log_{10} \tilde{K}$	$[-5,\ 0]$
$\log_{10} H_* R_*$	$[-3,\ 0]$
Geometric parameters	
$\log_{10} \Omega_b$	$[-30,\ -5]$
$\log_{10} f_b$	$[-10,\ 4]$
Spectral parameters	
a_1	$[0.2,\ 2.2]$
n_1	$[1.4,\ 3.4]$
n_2	$[-3.4,\ -1.4]$

results are summarized in Tables 5.2–5.4 (entries labeled as n/a correspond to posterior values that are not available or not applicable).

Figure 5.1 corresponds to the geometric parameters of the bubble collision template, while Figure 5.2 shows the thermodynamic parameters. The shown distributions are obtained from more than one million MCMC samples, where each sample corresponds to one combination of parameter values drawn from the prior ranges.

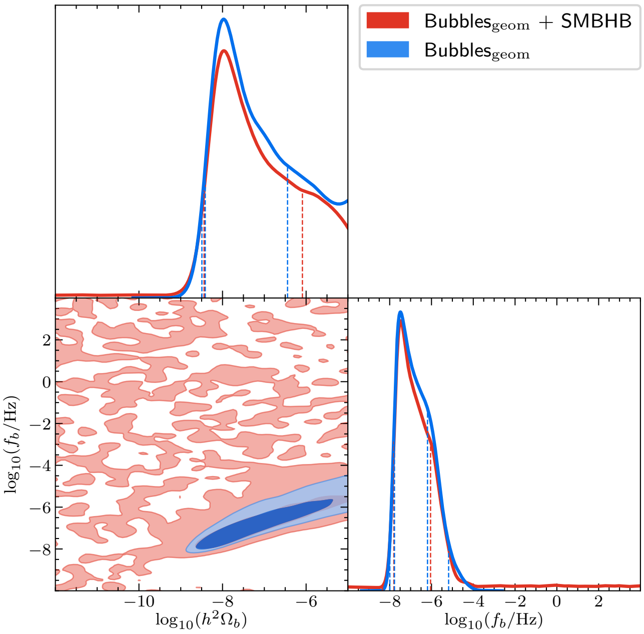

Figure 5.1: Posterior distributions for the geometric parameters $\{\Omega_b, f_b\}$ of the bubble collision template.

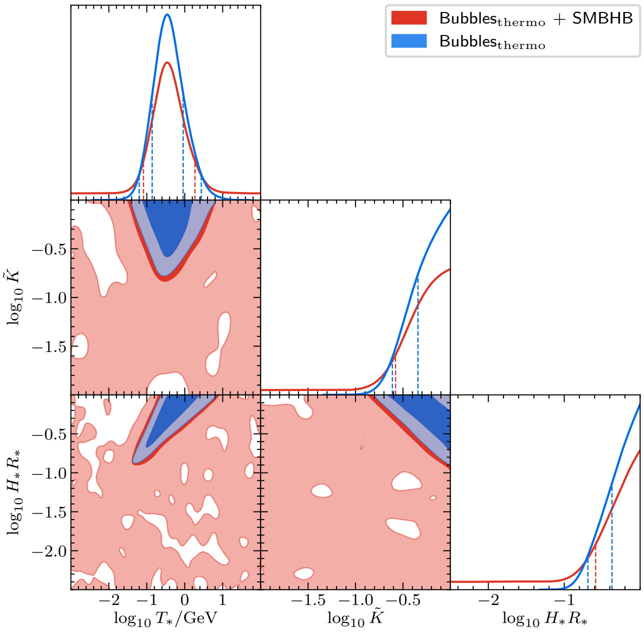

Figure 5.2: Posterior distributions for the thermodynamic parameters $\{T_*, \tilde{K}, H_*R_*\}$ of the bubble collision template.

Table 5.2: Credible intervals for geometric parameters (Bubbles).

Parameter	68% CI		95% CI	
	PT-BUBBLE	PT-BUBBLE+SMBHB	PT-BUBBLE	PT-BUBBLE+SMBHB
$h^2\Omega_b$	$[3.86 \times 10^{-9}, 3.60 \times 10^{-7}]$	$[3.62 \times 10^{-9}, 8.16 \times 10^{-7}]$	$> 3.21 \times 10^{-9}$	$> 2.10 \times 10^{-30}$
f_b (Hz)	$[1.69 \times 10^{-8}, 6.45 \times 10^{-7}]$	$[1.58 \times 10^{-8}, 9.04 \times 10^{-7}]$	$[1.02 \times 10^{-8}, 6.61 \times 10^{-6}]$	$> 4.52 \times 10^{-9}$
a_1	$[0.26, 1.52]$	$[0.45, 1.74]$	< 2.07	> 0.33
n_1	$[1.42, 2.46]$	$[1.46, 2.61]$	< 3.19	< 3.24
n_2	$[-2.80, -1.46]$	$[-2.81, -1.45]$	> -3.30	> -3.30

Table 5.3: Credible intervals for thermodynamic parameters (Bubbles).

Parameter	68% CI		95% CI	
	PT-BUBBLE+SMBHB	PT-BUBBLE	PT-BUBBLE+SMBHB	PT-BUBBLE
T_* (MeV)	$[8.17 \times 10^{1}, 1.86 \times 10^{3}]$	$[1.39 \times 10^{2}, 9.07 \times 10^{2}]$	$> 4.97 \times 10^{-1}$	$[6.31 \times 10^{1}, 2.73 \times 10^{3}]$
$\tilde{K}$	$> 2.64 \times 10^{-1}$	$> 4.55 \times 10^{-1}$	*n/a*	$> 2.45 \times 10^{-1}$
H_*R_*	$> 2.59 \times 10^{-1}$	$> 4.26 \times 10^{-1}$	*n/a*	$> 2.05 \times 10^{-1}$
a_1	$[0.83, 2.05]$	$[0.74, 1.92]$	> 0.39	> 0.48
n_1	$[1.95, 3.23]$	$[1.81, 3.04]$	> 1.54	> 1.56
n_2	< -1.45	< -2.06	< -1.41	*n/a*

Table 5.4: Maximum posterior values

Parameter	PT-BUBBLE+SMBHB	PT-BUBBLE
Geometric parameter		
$h^2\Omega_b$	1.08×10^{-8}	1.07×10^{-8}
f_b (Hz)	3.38×10^{-8}	3.25×10^{-8}
a_1	0.83	0.60
n_1	1.91	1.86
n_2	-2.12	-2.01
Thermodynamic parameter		
T_* (MeV)	345.00	346.00
$\tilde{K}$	1.00	1.00
H_*R_*	1.00	1.00
a_1	1.17	1.16
n_1	2.38	2.28
n_2	-1.66	-3.16

Figures 5.1 and 5.2, together with the credible intervals and maximum posterior values, show the following trends:

- The thermodynamic parameter $\tilde{K}$ is preferred to be close to unity, consistent with the assumption of a very strong FOPT ($\alpha \gg 1$).
- The average bubble separation H_*R_* tends to be large, approaching one, indicating that the data favor relatively large bubbles.
- The temperature at the end of the phase transition T_* is around $100\ \mathrm{MeV}$–$1\ \mathrm{GeV}$, in line with the QCD phase transition.
- The frequency f_b lies in the nanohertz band, making it relevant for PTA data, while the corresponding amplitude Ω_b falls within the range $\sim 10^{-10}$–10^{-6}, consistent with values preferred by NANOGrav observations.
- Comparing the posteriors with and without an SMBHB contribution, the key difference is that the inclusion of SMBHBs opens up parameter regions in which the PT signal is too weak to contribute significantly by itself. The SMBHB background does not directly depend on the thermodynamic or geometric PT parameters, but instead acts as an independent additive contribution to the spectrum, thereby mildly relaxing the constraints on the PT parameters.

Overall, these results suggest that the PTA data are consistent with strong FOPTs at QCD-like temperatures, producing a SGWB in the nanohertz frequency range, with large bubble sizes and high energy release.

The Figures 5.1 and 5.2 do not include the spectral parameters n_1, n_2 and a_1 to be more concise and clear. For the bubble template the figures including the spectral parameters are shown in the Appendix A. Physically, we expect $n_1 \sim 3$ on scales larger than the horizon due to causality, while n_2 should be negative to ensure a finite total energy. Because the NANOGrav data primarily probe the rising part of the spectrum, corresponding to the low-frequency slope, n_1 and also a_1 are still moderately constrained, whereas n_2, associated with the high-frequency slope, remains largely unconstrained, as evident from the posterior distributions in Appendix A. This behavior is similar for the other models. Given these broad posteriors, we will not discuss the spectral parameters in detail in the subsequent analysis of other templates, and will instead focus on the geometric and thermodynamic parameters.

5.2 Sound Waves

Following bubble collisions, compression waves propagate through the plasma and source GWs (this behaviour is captured by the sound shell model [32]). We model the resulting SGWB with a double broken power law (DBPL),

$$\Omega_{\mathrm{DBPL}}(f;\,\vec{\theta}_{\mathrm{cosmo}}) = \Omega_2\, S_2(f), \tag{5.7}$$

where Ω_2 denotes the amplitude at the second break frequency f_2, and

$$S(f) = N\left(\frac{f}{f_1}\right)^{n_1}\left[1+\left(\frac{f}{f_1}\right)^{a_1}\right]^{\frac{n_2-n_1}{a_1}}\left[1+\left(\frac{f}{f_2}\right)^{a_2}\right]^{\frac{n_3-n_2}{a_2}}, \tag{5.8}$$

with the shape

$$S_2(f) \equiv \frac{S(f)}{S(f_2)} \qquad \text{(so that } S_2(f_2)=1\text{)}. \tag{5.9}$$

Hence the spectrum scales roughly as f^{n_1} for $f < f_1$, f^{n_2} for $f_1 < f < f_2$, and f^{n_3} for $f > f_2$. The parameters a_1, a_2 control the width of the transition near the

spectral breaks.
The normalization constant N is defined by

$$\int_{-\infty}^{\infty} d\ln f \; S(f) = 1, \tag{5.10}$$

but by using at least Ω_2 and f_2 as our free geometric parametrisation the explicit evaluation of N is unnecessary, because N cancels in $S_2(f)$. The DBPL can also be written in terms of an integrated amplitude Ω_{int}, which is linked to the thermodynamic parameters:

$$\Omega_{\text{DBPL}}(f) = \Omega_{\text{int}}\, S(f). \tag{5.11}$$

For the specific choice of spectral slopes adopted in the LISA study the normalization N can be obtained analytically. In our analysis we do not fix those spectral slopes and allow them to vary, therefore N is not analytically computable across the full prior range. To use Equation 5.11 to constrain the thermodynamic parameters, N must be approximated. The approximation method is described in the following subsection 5.2.1.
The break frequencies are related to the thermodynamic parameters via:

$$f_1 \simeq 0.2\, H_{*,0}\, (H_* R_*)^{-1}, \tag{5.12}$$

$$f_2 \simeq 0.5\, H_{*,0}\, \Delta_w^{-1}\, (H_* R_*)^{-1}, \tag{5.13}$$

where $\Delta_w = \xi_{\text{shell}} / \max(v_w, c_s)$ encodes the dimensionless sound-shell thickness, specific to the sound wave model. ξ_{shell} can be expressed as

$$\xi_{\text{shell}} = |v_w - c_s|,$$

for all cases except $v_w = c_s$ (shell thickness would vanish). We set $c_s^2 = 1/3$.
The integrated amplitude is expressed as

$$h^2\Omega_{\text{int}} = h^2 F_{\text{GW},0}\, A_{\text{sw}}\, K^2\, (H_* \tau_{\text{sw}})\, (H_* R_*), \tag{5.14}$$

where $A_{\text{sw}} \simeq 0.11$ is a numerical factor and $K \simeq 0.6\, \kappa\, \alpha/(1+\alpha)$ is the kinetic energy fraction. κ denotes the kinetic energy fraction of a single expanding bubble. τ_{sw} is the duration of the sound wave source, which is also a new term in the scaling part of the GW spectrum specific to the sound wave model. It is expressed as:

$$H_* \tau_{\mathrm{sw}} = \min\bigl[H_* \tau_{\mathrm{sh}}, 1\bigr], \quad H_* \tau_{\mathrm{sh}} = \frac{H_* R_*}{\sqrt{\bar{v}_f^2}}, \tag{5.15}$$

where $\bar{v}_f^2 = \Gamma^{-1} K$ denotes the average squared fluid velocity and $\Gamma = 4/3$ the mean adiabatic index for a radiation fluid.

Priors. The priors for the geometric and thermodynamic parameters in this model are chosen by similar arguments to those in the bubble collision analysis, e.g. temperatures and frequencies are adapted to fit the PTA sensitivity band.
The previous assumption of a very strong PT ($v_w = 1$) is relaxed and the bubble wall velocity is treated as a free parameter ranging from 0.6 to 1. The full set of priors is listed in Table 5.5.

5.2.1 Normalization of the Double-Broken Power Law

In this analysis the spectral parameters are treated as free and allowed to vary over a wide prior range. As a consequence, N cannot be expressed in closed form for arbitrary parameter choices.

In principle, N could be determined numerically by integrating the DBPL shape function, which would give the most accurate result. However, this becomes computationally expensive because the normalization would have to be evaluated for every sample/prior combination inside the MCMC. Although a fully numerical evaluation was implemented, it was eventually discarded as infeasible within the scope of this Bachelor thesis, given our target of at least one million samples per model. For this reason we adopt an analytic approximation for N.

For compactness we write:

$$s(f) \equiv s(f; f_1, f_2, \{n_i\}, \{a_j\}), \qquad S(f) = N\, s(f),$$

Table 5.5: Prior ranges for the thermodynamic, geometric and spectral parameters of the sound-wave (SW) template.

Parameter	**Prior (Uniform)**
Thermodynamic parameters	
$\log_{10} K$	$[-4,\ -0.2]$
$\log_{10}(H_* R_*)$	$[-3,\ 0]$
v_w	$[0.6,\ 1]$
$\log_{10}(T_*/\mathrm{GeV})$	$[-4,\ 4]$
Geometric parameters	
$\log_{10}(h^2 \Omega_2^{\mathrm{sw}})$	$[-30,\ -5]$
$\log_{10}(f_2^{\mathrm{sw}}/\mathrm{Hz})$	$[-10,\ 4]$
$\log_{10}(f_2^{\mathrm{sw}}/f_1^{\mathrm{sw}})$	$[0,\ 2]$
Spectral parameters	
n_1	$[2,\ 4]$
n_2	$[0,\ 2]$
n_3	$[-4,\ -2]$
a_1	$[1,\ 3]$
a_2	$[3,\ 5]$

where $s(f)$ is the unnormalized DBPL, f_i are the frequency breaks and a_j, n_i the spectral parameters. We reintroduce the SBPL (similar to the definition in the bubble parametrization Equation 5.2), which is used for this approximation,

$$s_1(f; f_b, p, q, a) \equiv \left(\frac{f}{f_b}\right)^p \left[1 + \left(\frac{f}{f_b}\right)^a\right]^{\frac{q-p}{a}}. \tag{5.16}$$

To obtain a closed-form approximation for the normalization we construct a SBPL approximation that reproduces the high-frequency behaviour of S and then correct its low-frequency asymptotic. The approximation strategy is based on the observation that in the limit $f_1/f_2 \to 0$ the DBPL reduces to a SBPL. Define the scaled SBPL approximation

$$S_1(f) \equiv A\, s_1(f; f_2, n_2, n_3, a_2), \qquad A \equiv \frac{N\, s(f_2)}{s_1(f_2; f_2, n_2, n_3, a_2)}. \tag{5.17}$$

By construction $S_1(f_2) = S(f_2)$ and $S_1(f) \simeq S(f)$ for $f \gtrsim f_2$.
However $S_1(f \to 0) \propto (f/f_2)^{n_2}$ generally disagrees with the true low-frequency scaling $S(f \to 0) \propto (f/f_1)^{n_1}$ since $n_1 > n_2$. We therefore introduce the piecewise-corrected approximation

$$\widetilde{S}_1(f) = \begin{cases} S_1(f) - A\left(\dfrac{f}{f_2}\right)^{n_2} + X(f), & f \le f_c, \\ S_1(f), & f > f_c, \end{cases} \tag{5.18}$$

where $X(f)$ restores the correct low-frequency asymptotic,

$$X(f \to 0) = N\left(\frac{f}{f_1}\right)^{n_1}. \tag{5.19}$$

We consider two pragmatic choices for $X(f)$ (only the first is used in the remainder of this thesis):

- ▷ **PL correction:** $X(f) = N\,(f/f_1)^{n_1}$. For this ansatz continuity $\widetilde{S}_1(f_c) = S_1(f_c)$ implies the matching relation

$$A\left(\frac{f_c}{f_2}\right)^{n_2} = N\left(\frac{f_c}{f_1}\right)^{n_1} . \tag{5.20}$$

- ▷ **SBPL correction:** $X(f) = \tilde{A}\,s_1(f; f_1, n_1, n_2, a_1)$ with $\tilde{A}$ chosen such that $X(f_1) = S(f_1)$.

To calculate N we split the $\ln x$ integral in Equation 5.10 at $\ln(f_c/f_1)$ and compute the part above f_c using the SBPL S_1. For $f < f_c$ we correct the wrong low-frequency asymptotic of S_1 by subtracting its $(f/f_2)^{n_2}$ term and adding the correct asymptote in the form of $X(f)$, chosen either as a simple power law or as an SBPL. This leads to an expression for $1/N$ consisting of the SBPL contribution at high f and the added low-frequency correction. The full algebraic steps are skipped here for clarity but are provided in the Appendix section B.1.

Using the analytic SBPL integral and the PL correction we obtain the practical expression:

$$\frac{1}{N} \simeq \frac{s(f_2)}{s_1(f_2; f_2, n_2, n_3, a_2)}\left[\frac{\Gamma(n_2/a_2)\,\Gamma(|n_3|/a_2)}{a_2\,\Gamma((n_2+|n_3|)/a_2)} - \frac{1}{n_2}\left(\frac{f_c}{f_2}\right)^{n_2}\right] + \frac{1}{n_1}\left(\frac{f_c}{f_1}\right)^{n_1} . \tag{5.21}$$

N can similarly be calculated for the SBPL approximation. In that case we obtain an expression involving the hypergeometric function ${}_2F_1$, whose numerical evaluation becomes computationally expensive when repeated on the order of 10^6 times. To illustrate and compare the two approximation methods, a representative parameter set from within the prior range was chosen: $f_2 = 4 \times 10^{-8}\,\mathrm{Hz}$, $f_1 = f_2/10$, $n_1 = 3$, $n_2 = 1$, $n_3 = -3$, $a_1 = 2$, $a_2 = 4$. In Figure 5.3 we compare the approximations with the DBPL on a log-log scale and log-linear scale.

In Figure 5.3, the differences between the two approximation methods are clearly visible. The SBPL approximation $\tilde{S}_1$ (SBPL corr.) lies almost entirely on top of the original DBPL, effectively covering it. In contrast, $\tilde{S}_1$ (PL corr.) approaches f_c^{PL} from higher frequencies as S_1, and provides a good approximation of the DBPL shape at

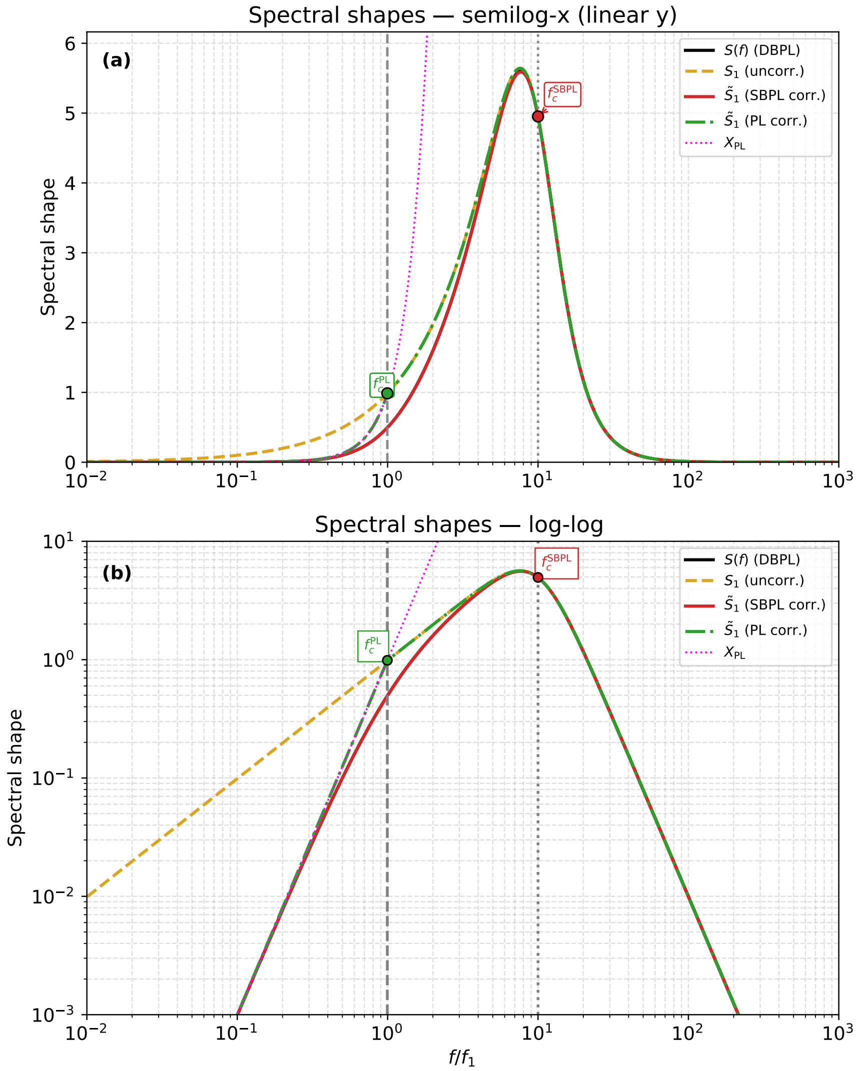

Figure 5.3: Comparison of the DBPL shape $S(f)$ with its approximations $\tilde{S}_1$ (SBPL corr.) and $\tilde{S}_1$ (PL corr.). Plots are on (a) semilogarithmic (linear y-axis) scale and (b) double-logarithmic scale. All shape functions are rescaled so they are independent of N (all original terms scaled by $1/N$).

high frequencies. However, the accuracy deteriorates as it approaches $f_c^{\rm PL}$. At this point, the behavior transitions from SBPL-like to PL-like, and the approximation gradually converges back toward the DBPL shape at lower frequencies.

In particular, around f_c^{PL}, $\tilde{S}_1$ (PL corr.) overestimates the actual shape function, resulting in a less accurate approximation compared to $\tilde{S}_1$ (SBPL corr.). Despite the overall higher accuracy of the SBPL approximation, the PL approximation was employed in this thesis due to the lower computational cost, which was more suitable within the scope of this work.

5.2.2 Posterior Distributions and Parameter Constraints

Posterior distributions for both the geometric parameters and the corresponding thermodynamic parameters for the sound wave model are presented below. The numerical results are summarized in Tables A.1–A.3 in the appendix.

Figure 5.4 corresponds to the geometric parameters of the sound wave template, while Figure 5.5 shows the thermodynamic parameters. The shown distributions are again obtained from more than 10^6 MCMC samples.

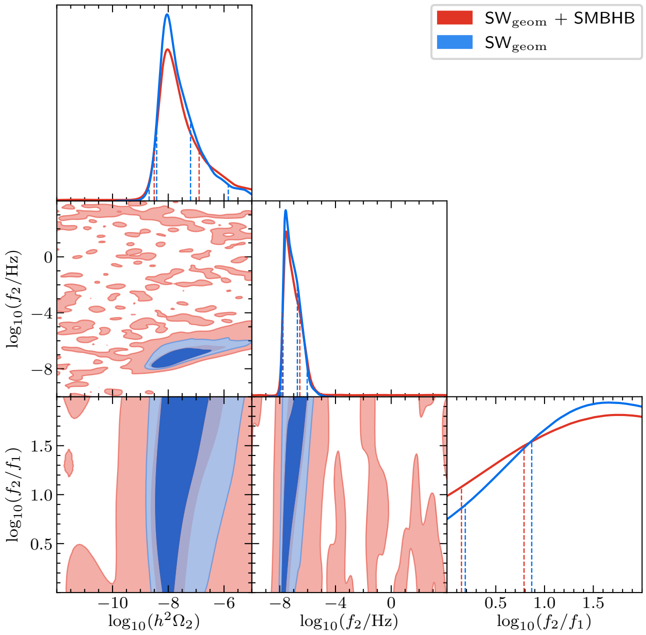

Figure 5.4: Posterior distributions for the geometric parameters $\{\Omega_2^{\mathrm{sw}},\ f_2^{\mathrm{sw}},\ f_2^{\mathrm{sw}}/f_1^{\mathrm{sw}}\}$ of the sound wave template.

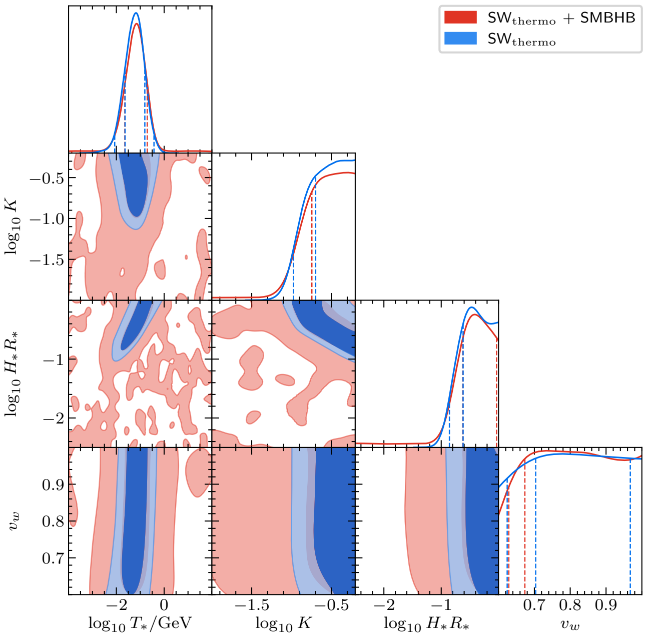

Figure 5.5: Posterior distributions for the thermodynamic parameters $\{T_*, K, H_*R_*\, v_w\}$ of the sound wave template.

Figures 5.4 and 5.5 summarise the posterior results. The maximum posterior values without SMBHB (with SMBHB) are

$$\begin{aligned} T_*^{(\mathrm{SW})} &= 65.70\ (70.69)\,\mathrm{MeV}, & T_*^{(\mathrm{BUBBLE})} &= 346.00\ (345.00)\,\mathrm{MeV}, \\ K^{(\mathrm{SW})} &= 0.63\ (0.50), & \tilde{K}^{(\mathrm{BUBBLE})} &= 1.00\ (1.00), \\ H_*R_*^{(\mathrm{SW})} &= 0.34\ (0.39), & H_*R_*^{(\mathrm{BUBBLE})} &= 1.00\ (1.00), \end{aligned}$$

and for the wall velocity (SW only)

$$v_w^{(\mathrm{SW})} = 0.77\ (0.73).$$

The wall velocity v_w is only weakly constrained. This is likely because v_w only affects the ratio f_2/f_1, which carries little posterior information. Geometrically, this can be understood from the fact that the NANOGrav data currently exhibit essentially a single power-law slope, starting around $10^{-9}\,\mathrm{Hz}$ and extending up to about $5 \times 10^{-8}\,\mathrm{Hz}$. Positioning either f_1 or f_2 at the turnover of this slope and adjusting the corresponding spectral slope already provides a good fit to the data, leaving freedom for the second peak. Thus, the weak constraint on v_w mainly reflects that the present data are consistent with a single slope rather than two distinct spectral features.

Overall, the maximum-posterior values indicate systematically higher temperatures and larger characteristic scales in the bubble model than in the SW model, but these offsets are not decisive given the overlapping credible intervals. $K^{(\mathrm{SW})}$ again peaks at the higher end of the prior range indication that high kinetic energy fractions are preferred by the data. The geometric frequencies and amplitude are consistent with NANOGrav observations and the general trend of all parameters are the same for both the bubble and SW model.

5.3 Sound Waves and Turbulence

Magnetohydrodynamic (MHD) turbulence in the primordial plasma represents a significant mechanism for the generation of GWs during FOPTs. This mechanism involves a combination of anisotropic stresses produced by fluid velocity and magnetic fields. Historically, turbulence was frequently overlooked in earlier analyses, mainly due to its presumed subdominance and the lack of a simulation-validated templates for its SGWB spectrum. However, its significance as a source is now recognized, particularly if the lifetime of sound waves proves shorter than one Hubble time. A simulation-validated template for the SGWB produced by turbulence has since been developed and is utilized in this analysis.

The total energy density fraction in the GW source from turbulence is defined as:

$$\Omega_s \equiv \Omega_{\text{kin}} + \Omega_{\text{mag}} = \varepsilon\, K, \tag{5.22}$$

where K is the kinetic energy fraction of the fluid, and ε represents the fraction of the overall kinetic energy in bulk fluid motion that is converted into MHD turbulence.

A key assumption here is rapid equipartition between the turbulent kinetic and magnetic energies, such that $\Omega_{\text{mag}} \approx \Omega_{\text{kin}}$. Under this assumption, the characteristic fluid velocity $\bar{v}_f$ and Alfvén speed $\bar{v}_A$ are related to Ω_s by

$$\bar{v}_f^2 \approx \bar{v}_A^2 \approx \Gamma^{-1}\varepsilon K = \frac{3}{4}\Omega_s \tag{5.23}$$

for $\Gamma = 4/3$. The SGWB from MHD turbulence is also modeled by a DBPL spectrum. In contrast to the sound wave model, a distinguishing feature of turbulent motion in the plasma is that the ratio of the break frequencies, f_2/f_1, is generally large, with $f_2/f_1 \gtrsim 5$. More specifically, this ratio is approximately given by $\frac{f_2}{f_1} = 2.2\mathcal{N}/\,\bar{v}_A \simeq 2.5\mathcal{N}/\,\sqrt{\Omega_s}$ for $\mathcal{N} \simeq 2$ eddy turnover times. When the spectrum is then approximated again as an SBPL for frequencies $f/f_1 \gg 1$ an expression for Ω_2 can be found, thus allowing for the usage of Equation 5.7 and avoiding the normalization approximation for N.

The final expression for the SGWB spectrum generated by turbulence is given by:

$$\Omega^{\text{GW}}_{\text{MHD}}(f) = \frac{3A\bar{v}A\Omega_s^2(H_*R_*)^2F_{\text{GW},0}}{4\pi^2N}\left(\frac{f}{f_1}\right)^{n_1}\left[1+\left(\frac{f}{f_1}\right)^{a_1}\right]^{\frac{-n_1+n_2}{a_1}}\left[1+\left(\frac{f}{f_2}\right)^{a_2}\right]^{\frac{-n_2+n_3}{a_2}}. \tag{5.24}$$

Here, $A \simeq 0.085$ is a numerical amplitude factor.

The first and second break frequencies f_1 and f_2 are explicitly related to thermodynamic parameters:

$$f_1 = \frac{\sqrt{3\Omega_s}}{2\mathcal{N}}H_{*,0}(H_*R_*)^{-1}, \tag{5.25}$$

$$f_2 \simeq 2.2H_{*,0}(H_*R_*)^{-1}. \tag{5.26}$$

So we characterize the spectrum by the thermodynamic parameters $\{K, H_*R_*, T_*, \varepsilon\}$.

In the LISA analysis it is assumed that both sound waves and turbulence contribute to GW production. The total spectrum of the SGWB,$\Omega_{\text{GW}}(f)$, is composed of the superposition of their individual contributions. This is modeled by summing the two DBPL templates. The combined spectrum $\Omega_{\text{GW}}(f)$ is therefore expressed as:

$$\Omega_{\text{GW}}(f) = \Omega_{\text{turb}}(f) + \Omega_{\text{sw}}(f).$$

The following priors were used for the combined spectrum:

Table 5.6: Prior ranges for the thermodynamic and spectral parameters of the combined sound waves and turbulence template.

(a) Thermodynamic & geometric priors

Parameter	**Prior (Uniform)**
Thermodynamic parameters	
$\log_{10} T_*$	[-4, 4]
$\log_{10} K$	[-4, -0.2]
$\log_{10} H_*R_*$	[-3, 0]
v_w	[0.6, 1]
ε	[0.01, 1.2]
Geometric parameters	
$\log_{10}\left(h^2\Omega_2^{\rm sw}\right)$	[-30, -5]
$\log_{10}\left(\Omega_2^{\rm turb}/\Omega_2^{\rm sw}\right)$	[-5, 0]
$\log_{10}(f_2^{\rm sw}/{\rm Hz})$	[-10, 4]
$\log_{10}(f_2^{\rm sw}/f_1^{\rm sw})$	[0, 2]
$\log_{10}\left(f_1^{\rm turb}/f_1^{\rm sw}\right)$	[-2, 2]

(b) Spectral priors

Parameter	**Prior (Uniform)**
Turbulence spectral parameters	
a_1	[3, 5]
a_2	[1.15, 3.15]
n_1	[2, 4]
n_2	[0.1, 2]
n_3	[-11/3, -5/3]
Sound-wave spectral parameters	
$a_{1,\rm sw}$	[1, 3]
$a_{2,\rm sw}$	[3, 5]
$n_{1,\rm sw}$	[2, 4]
$n_{2,\rm sw}$	[0.1, 2]
$n_{3,\rm sw}$	[-4, -2]

Notes. The ratio $f_2^{\rm turb}/f_1^{\rm sw}$ is additionally fixed to 11.

5.3.1 Posterior Distributions and Parameter Constraints

Posterior distributions for both the geometric parameters and the corresponding thermodynamic parameters for the sound wave + turbulence model are presented below. The numerical results are summarized in Tables A.4–A.6 in the appendix.

Figure 5.6 corresponds to the geometric parameters of the sound wave + turbulence template, while Figure 5.7 shows the thermodynamic parameters. The distribution shown in Figure 5.7 is based on more than 10^6 MCMC samples, while Figure 5.6 only relies on about 6×10^5 samples due to some technical issues during the preparation phase of this bachelor thesis. Nevertheless, the general trends are clearly visible already with 6×10^5 samples.

Figure 5.7 and Figure 5.6 show that the inclusion of the turbulence component does not significantly alter the results compared to the pure SW model. The maximum-posterior values illustrate this similarity. For example, the temperature at the end of

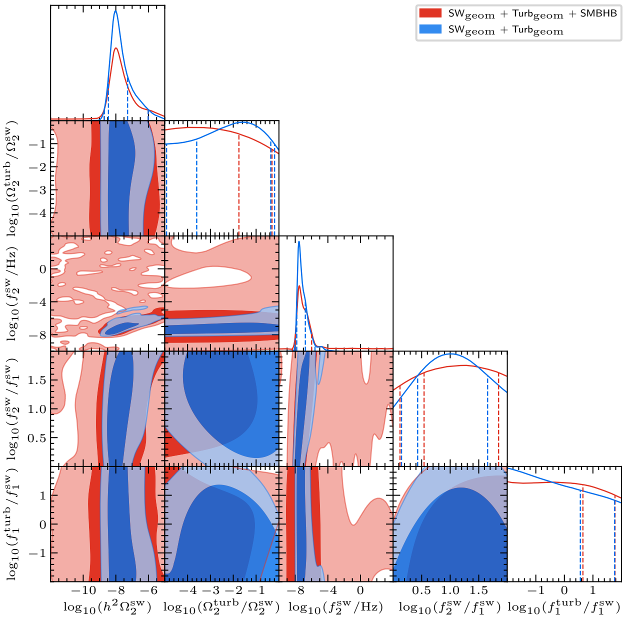

Figure 5.6: Posterior distributions for the geometric parameters $\{\log_{10}(h^2\Omega_2^{\rm sw}), \ldots, \log_{10}(f_1^{\rm turb}/f_1^{\rm sw})\}$ (sound wave + turbulence model).

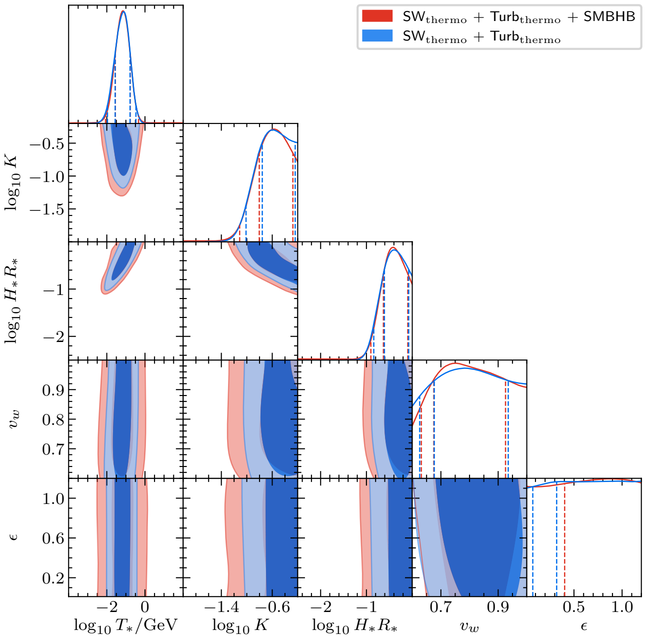

Figure 5.7: Posterior distributions for the thermodynamic parameters $\{T_*, K, H_*R_*, v_w, \varepsilon\}$ of the sound wave + turbulence template.

the transition $T_* = 76.94\,\mathrm{MeV}$ ($70.16\,\mathrm{MeV}$) is very close to the SW-only case. H_*R_* and v_w show similar trends. K has a smaller maximum posterior at around 0.25 (0.27) and a more defined peak has evolved, meaning the inclusion of turbulences seem to favour weaker PTs compared to the SW-only model or at least the kinetic energy fraction seems to be lower. This is somewhat unexpected, since turbulence is usually associated with more energetic scenarios, where a larger fraction of the released vacuum energy is converted into bulk motion of the plasma.

The new turbulence parameter ε is not meaningfully constrained as the credible intervals extend down to very small values. This weak sensitivity explains why the addition of turbulence has only a marginal impact on the other thermodynamic parameters: at all values of ε shifts in that parameter can be effectively compensated by small changes in other parameters, like H_*R_* or K.

The impact of the SMBHB spectrum on the SW + turbulence thermodynamic parameters differs from the other two models. The parameter space still gets wider and more points are allowed but only in the direct vicinity of the space occupied by the PT-only model. Regions of parameter space far from the main posterior peaks remain unpopulated, indicating that the inclusion of SMBHBs alone is insufficient to make these areas compatible with the data. The model contribution in these regions remains too weak, particularly compared to the other models.

The geometric parameters again fit to the NANOGrav prediction, but the ratios $\Omega_2^{\mathrm{turb}}/\Omega_2^{\mathrm{sw}}$ and $f_2^{\mathrm{sw}}/f_1^{\mathrm{sw}}$ are not well constrained. Overall with the inclusion of SMBHBs no meaningful constraints can be extrapolated in this case, as the model has too many degrees of freedom.

To conclude the SW+Turb results are very close to the SW-only case, indicating that the NANOGrav signal has negligible constraining power for the turbulence sector.

Summary and Outlook

6

In this Bachelor's thesis, we utilized the PTArcade framework and the NANOGrav 15-year dataset to constrain thermodynamic and geometric parameters of First-Order Phase Transitions (FOPTs) as a source for the stochastic gravitational wave background (SGWB) observed by Pulsar Timing Arrays (PTAs). We fitted theoretical gravitational wave spectrum templates corresponding to different FOPT mechanisms: bubble collisions, sound waves, and a combination of sound waves and magnetohydrodynamic turbulence. Our investigations consistently showed that the observed SGWB signal is plausibly explained by strong FOPTs in the early universe. These phase transitions likely occurred at temperatures ranging from approximately 100 MeV to 1 GeV, a scale broadly compatible with the QCD phase transition. The derived gravitational wave spectra consistently showed peak frequencies in the nanohertz band, with amplitudes consistent with NANOGrav observations. Across all models, the data favored energetic FOPTs where a substantial fraction of latent heat was converted into kinetic energy and the formation of relatively large bubbles (characterized by large mean bubble separation H_*R_* and fractional energy density K or $\tilde{K}$ approaching unity). While these broad characteristics were common, distinct differences and limitations emerged for individual models:

- For the bubble collision model, the NANOGrav data strongly favored very strong FOPTs with a fractional energy density $\tilde{K}$ close to unity, implying a high α (ratio of vacuum to radiation energy density). The mean bubble separation H_*R_* also tended to be large. While the low-frequency spectral slope (n_1) and smoothness parameter (a_1) were moderately constrained, the high-frequency slope (n_2) remained largely unconstrained (this behavior is similar for the other models). The inclusion of a Supermassive Black Hole Binary (SMBHB) foreground opened up more parameter regions, thereby relaxing constraints on the FOPT signal.

- ▷ The sound wave model also yielded consistent geometric frequencies and amplitudes. However, it suggested systematically lower maximum posterior values for the transition temperature (T_*) and relative bubble separation (H_*R_*) compared to the bubble collision model. Despite these differences, the substantial overlap of their credible intervals means that the two models cannot be clearly distinguished. The bubble-wall velocity (v_w) was only weakly constrained, because it only effects the second break frequency, for which the current data provide little constraint.
- ▷ The sound wave and turbulence model did not show significant alterations in its overall results compared to the pure sound wave model. Maximum posterior values for T_*, H_*R_*, and v_w remained similar. The kinetic energy fraction K was slightly smaller, potentially favoring weaker phase transitions (unexpected, as turbulence is usually associated with more energetic scenarios). Most notably, the turbulence fraction, ε, was not meaningfully constrained, indicating that the NANOGrav signal had negligible constraining power for the turbulence model. This implies that the current PTA data are not sensitive enough to constrain the specific contribution of MHD turbulence.

In summary, all FOPT models offer a plausible explanation for the nanohertz SGWB, but current PTA data primarily constrain the overall energy scale, bubble separation and characteristic frequencies, leaving more detailed model specific parameters (like specific wall velocities, or turbulence fractions) and high-frequency spectral slopes largely unconstrained.

The FOPT models implemented and analyzed in this work, including those for bubble collisions, sound waves and turbulence, can be directly applied to these next generation PTA datasets (like the NANOGrav 20-year data set). These releases contain a larger number of pulsars, enabling more cross-correlations, and have increased sensitivity to lower frequencies ($f_{\rm min} \sim 1/T_{\rm obs}$) through a longer observation span. These improvements can lead to better constraints. Such improvements would enable a more detailed understanding of the microphysical processes driving phase transitions. In particular, distinguishing between different FOPT mechanisms, assuming such transitions occurred, will require higher-precision PTA measurements and improved theoretical modeling. If the signal does not originate from a FOPT, these data mainly provide constraints on what scenarios are excluded.

Appendix

A

Here the cornerplots for the bubble-collision template including the spectral parameters are shown.

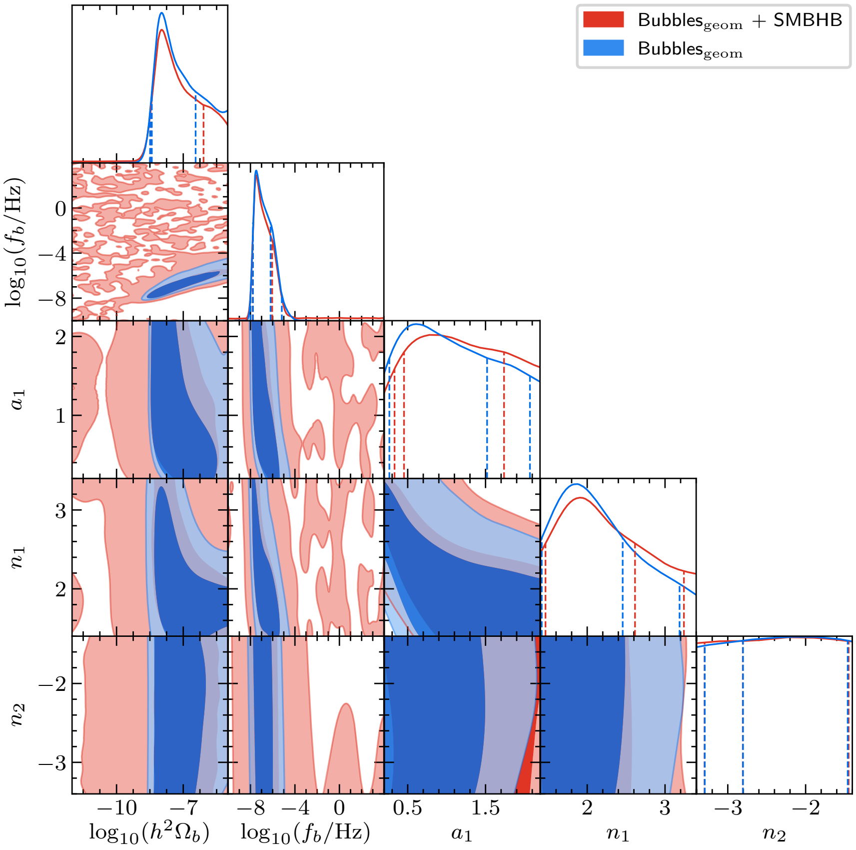

Figure A.1: Posterior distributions for the geometric parameters $\{\Omega_b, f_b\}$ of the bubble collision template including spectral parameters n_1, n_2 and a_1.

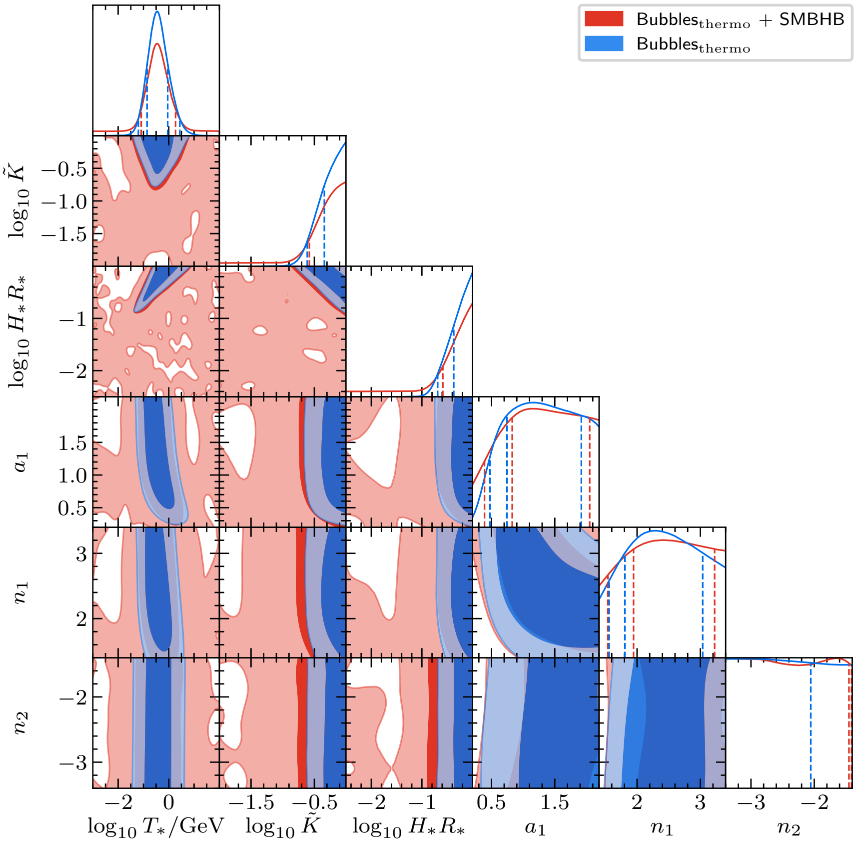

Figure A.2: Posterior distributions for the thermodynamic parameters $\{T_*, \tilde{K}, H_* R_*\}$ of the bubble collision template including spectral parameters n_1, n_2 and a_1.

A.1 Parameter Constraints Sound Wave Model

Table A.1: Credible intervals for geometric parameters (SW).

Parameter	68% CI		95% CI	
	PT-SW+SMBHB	PT-SW	PT-SW+SMBHB	PT-SW
$h^2\Omega_2$	$[3.12\times10^{-9},\,1.28\times10^{-7}]$	$[3.84\times10^{-9},\,6.30\times10^{-8}]$	*n/a*	$[2.05\times10^{-9},\,1.42\times10^{-6}]$
f_2 (Hz)	$[1.60\times10^{-8},\,2.76\times10^{-7}]$	$[1.71\times10^{-8},\,1.84\times10^{-7}]$	$[5.53\times10^{-9},\,6.75\times10^{3}]$	$[1.25\times10^{-8},\,9.29\times10^{-7}]$
f_2/f_1	> 6.16	> 7.39	> 1.41	> 1.54

Table A.2: Credible intervals for thermodynamic parameters (SW).

Parameter	68% CI		95% CI	
	PT-SW+SMBHB	PT-SW	PT-SW+SMBHB	PT-SW
T_* (MeV)	$[2.28\times10^{1},\,1.96\times10^{2}]$	$[2.32\times10^{1},\,1.56\times10^{2}]$	$[1.36\times10^{-1},\,1.20\times10^{6}]$	$[8.55\times10^{0},\,3.76\times10^{2}]$
$\tilde{K}$	$> 1.80\times10^{-1}$	$> 2.01\times10^{-1}$	$> 2.77\times10^{-4}$	$> 1.06\times10^{-1}$
H_*R_*	$[2.39\times10^{-1},\,9.26\times10^{-1}]$	$> 2.41\times10^{-1}$	$> 2.19\times10^{-3}$	$> 1.39\times10^{-1}$
v_w	> 0.67	$[0.70,\,0.97]$	> 0.63	> 0.62

Table A.3: Maximum posterior values — SW

Parameter	PT-SW+SMBHB	PT-SW
Geometric parameters		
$h^2\Omega_2$	9.46×10^{-9}	8.95×10^{-9}
f_2 (Hz)	2.85×10^{-8}	2.65×10^{-8}
f_2/f_1	57.32	45.63
Thermodynamic parameters		
T_* (MeV)	70.69	65.70
$\tilde{K}$	0.50	0.63
H_*R_*	0.39	0.34
v_w	0.73	0.78

A.2 Parameter Constraints Sound Wave and Turbulence Model

Table A.4: Credible intervals for geometric parameters (SW + Turb).

Parameter	68% CI		95% CI	
	SW+TURB+SMBHB	SW+TURB	SW+TURB+SMBHB	SW+TURB
$h^2\Omega_2^{\rm sw}$	$[1.92 \times 10^{-9},\, 9.84 \times 10^{-7}]$	$[3.52 \times 10^{-9},\, 5.25 \times 10^{-8}]$	$> 2.27 \times 10^{-30}$	$[1.96 \times 10^{-9},\, 9.64 \times 10^{-7}]$
$\Omega_2^{\rm turb}/\Omega_2^{\rm sw}$	$< 1.77 \times 10^{-2}$	$[2.50 \times 10^{-4},\, 4.39 \times 10^{-1}]$	$< 4.98 \times 10^{-1}$	$[1.20 \times 10^{-5},\, 6.44 \times 10^{-1}]$
$f_2^{\rm sw}$ (Hz)	$[1.08 \times 10^{-8},\, 1.02 \times 10^{-6}]$	$[1.52 \times 10^{-8},\, 1.73 \times 10^{-7}]$	$> 4.39 \times 10^{-9}$	$[9.28 \times 10^{-9},\, 2.63 \times 10^{-6}]$
$f_2^{\rm sw}/f_1^{\rm sw}$	$[3.49,\, 7.04 \times 10^{1}]$	$[2.69,\, 4.52 \times 10^{1}]$	> 1.32	> 1.40
$f_1^{\rm turb}/f_1^{\rm sw}$	< 4.46	< 3.63	$< 5.94 \times 10^{1}$	$< 5.75 \times 10^{1}$

Table A.5: Credible intervals for thermodynamic parameters (SW + Turb).

Parameter	68% CI		95% CI	
	SW+TURB+SMBHB	SW+TURB	SW+TURB+SMBHB	SW+TURB
T_* (MeV)	$[27.79,\, 167.29]$	$[27.38,\, 164.98]$	$[8.56,\, 460.35]$	$[10.86,\, 335.99]$
$\tilde{K}$	$[0.16,\, 0.53]$	$[0.18,\, 0.58]$	> 0.08	> 0.10
H_*R_*	$[0.23,\, 0.80]$	$[0.25,\, 0.84]$	> 0.13	> 0.14
ξ_w	$[0.68,\, 0.93]$	$[0.68,\, 0.94]$	> 0.63	> 0.63
ε	> 0.40	> 0.32	*n/a*	> 0.07

Table A.6: Maximum posterior values — SW + Turb.

Geometric parameters		
Parameter	SW+TURB+SMBHB	SW+TURB
$h^2\Omega_2^{\rm sw}$	1.01×10^{-8}	9.44×10^{-9}
$\Omega_2^{\rm turb}/\Omega_2^{\rm sw}$	2.18×10^{-4}	2.56×10^{-2}
$f_2^{\rm sw}$ (Hz)	3.06×10^{-8}	2.87×10^{-8}
$f_2^{\rm sw}/f_1^{\rm sw}$	1.85×10^{1}	1.04×10^{1}
$f_1^{\rm turb}/f_1^{\rm sw}$	1.00×10^{-2}	1.00×10^{-2}
Thermodynamic parameters		
T_* (MeV)	70.16	76.94
$\tilde{K}$	0.27	0.25
H_*R_*	0.38	0.40
v_w	0.75	0.78
ε	0.87	0.86

Appendix

B

B.1 Approximate Normalization Integral

We outline the steps used to obtain the approximate expression for $1/N$ quoted in the main text under the PL ansatz. For clarity, the integrals are rewritten in terms of the dimensionless variable x, so that the logarithmic integration limits involve only dimensionless quantities.

$$\begin{aligned}
\frac{1}{N} &= \frac{1}{N}\int_{-\infty}^{\infty} \mathrm{d}\ln x\; S(xf_1, f_1, f_2, \{n_i\}, \{a_j\}) && \text{(B.1)}\\
&\simeq \frac{1}{N}\int_{-\infty}^{\infty} \mathrm{d}\ln x\; \widetilde{S}_1(xf_1, f_1, f_2, \{n_i\}, \{a_j\}) && \text{(B.2)}\\
&= \frac{A}{N}\left[\int_{-\infty}^{\infty} \mathrm{d}\ln x\; s_1(xf_1, f_2, n_2, n_3, a_2) - \left(\frac{f_1}{f_2}\right)^{n_2}\int_{-\infty}^{\ln(f_c/f_1)} \mathrm{d}\ln x\; x^{n_2}\right] \\
&\quad + \frac{1}{N}\int_{-\infty}^{\ln(f_c/f_1)} \mathrm{d}\ln x\; X(xf_1, f_1, f_2, \{n_i\}, \{a_j\}) && \text{(B.3)}\\
&= \frac{A}{N}\left[\int_{-\infty}^{\infty} \mathrm{d}\ln x\; s_1(xf_1, f_2, n_2, n_3, a_2) - \frac{1}{n_2}\left(\frac{f_c}{f_2}\right)^{n_2}\right] + \frac{1}{N}\int_{-\infty}^{\ln(f_c/f_1)} \mathrm{d}\ln x\; X(xf_1, \dots). && \text{(B.4)}
\end{aligned}$$

The SBPL integral can be evaluated analytically.

$$\int_{-\infty}^{\infty} \mathrm{d}\ln x\; x^{p}\big(1 + x^{a}\big)^{\frac{q-p}{a}} = \frac{\Gamma(p/a)\,\Gamma(|q|/a)}{a\,\Gamma((p+|q|)/a)}, \tag{B.5}$$

with $p = n_2$, $q = n_3 < 0$ and $a = a_2$, one obtains

$$\int_{-\infty}^{\infty} \mathrm{d}\ln x \; s_1(xf_1, f_2, n_2, n_3, a_2) = \frac{\Gamma(n_2/a_2)\,\Gamma(|n_3|/a_2)}{a_2\,\Gamma((n_2 + |n_3|)/a_2)} \equiv I_{\mathrm{SBPL}}. \tag{B.6}$$

For the PL choice $X(f) = N(f/f_1)^{n_1}$ the remaining low-frequency integral evaluates to

$$\int_{-\infty}^{\ln(f_c/f_1)} \mathrm{d}\ln x \; \frac{X(xf_1)}{N} = \frac{1}{n_1}\left(\frac{f_c}{f_1}\right)^{n_1}. \tag{B.7}$$

Combining these results and using $A = Ns(f_2)/s_1(f_2)$ yields the expression quoted in the main text,

$$\frac{1}{N} \simeq \frac{s(f_2)}{s_1(f_2)}\left[I_{\mathrm{SBPL}} - \frac{1}{n_2}\left(\frac{f_c}{f_2}\right)^{n_2}\right] + \frac{1}{n_1}\left(\frac{f_c}{f_1}\right)^{n_1}. \tag{B.8}$$

Bibliography

[1] Albert Einstein. “Näherungsweise Integration der Feldgleichungen der Gravitation”. In: *Sitzungsberichte der Königlich Preußischen Akademie der Wissenschaften zu Berlin* (1916), pp. 688–696.

[2] R. A. Hulse and J. H. Taylor. “Discovery of a pulsar in a binary system”. In: *The Astrophysical Journal* 195 (1975), pp. L51–L53. DOI: `10.1086/181708`.

[3] B. P. Abbott et al. (LIGO Scientific Collaboration and Virgo Collaboration). “Observation of Gravitational Waves from a Binary Black Hole Merger”. In: *Physical Review Letters* 116.6 (2016), p. 061102. DOI: `10.1103/PhysRevLett.116.061102`.

[4] B. P. Abbott et al. (LIGO Scientific Collaboration and Virgo Collaboration). “Observation of Gravitational Waves from a Binary Neutron Star Inspiral”. In: *Physical Review Letters* 119.6 (2017), p. 161101. DOI: `10.1103/PhysRevLett.119.161101`.

[5] Daniel J. Reardon et al. “Search for an Isotropic Gravitational-wave Background with the Parkes Pulsar Timing Array”. In: *The Astrophysical Journal Letters* 951.1 (June 2023), p. L6. ISSN: 2041-8213. DOI: `10.3847/2041-8213/acdd02`. URL: `http://dx.doi.org/10.3847/2041-8213/acdd02`.

[6] Heng Xu et al. “Searching for the Nano-Hertz Stochastic Gravitational Wave Background with the Chinese Pulsar Timing Array Data Release I”. In: *Research in Astronomy and Astrophysics* 23.7 (June 2023), p. 075024. ISSN: 1674-4527. DOI: `10.1088/1674-4527/acdfa5`. URL: `http://dx.doi.org/10.1088/1674-4527/acdfa5`.

[7] J. Antoniadis et al. “The second data release from the European Pulsar Timing Array: III. Search for gravitational wave signals”. In: *Astronomy & Astrophysics* 678 (Oct. 2023), A50. ISSN: 1432-0746. DOI: `10.1051/0004-6361/202346844`. URL: `http://dx.doi.org/10.1051/0004-6361/202346844`.

[8] Gabriella Agazie et al. “The NANOGrav 15 yr Data Set: Evidence for a Gravitational-wave Background”. In: *The Astrophysical Journal Letters* 951.1 (June 2023), p. L8. ISSN: 2041-8213. DOI: `10.3847/2041-8213/acdac6`. URL: `http://dx.doi.org/10.3847/2041-8213/acdac6`.

[9] Matthew T Miles et al. “The MeerKAT Pulsar Timing Array: the first search for gravitational waves with the MeerKAT radio telescope”. In: *Monthly Notices of the Royal Astronomical Society* 536.2 (Dec. 2024), pp. 1489–1500. ISSN: 1365-2966. DOI: `10.1093/mnras/stae2571`. URL: `http://dx.doi.org/10.1093/mnras/stae2571`.

[10] The International Pulsar Timing Array Collaboration. “Comparing recent PTA results on the nanohertz stochastic gravitational wave background”. In: *arXiv preprint* (2023). https://arxiv.org/abs/2309.00693. arXiv: `2309.00693 [astro-ph.HE]`.

[11] Stephen R. Taylor. “The Nanohertz Gravitational Wave Astronomer”. In: *arXiv preprint* (2021). arXiv: `2105.13270 [astro-ph.IM]`. URL: `https://arxiv.org/abs/2105.13270`.

[12] Djuna Lize Croon and David James Weir. “Gravitational Waves from Phase Transitions”. In: *Contemporary Physics* 65.1 (2024), p. 75. DOI: `10.1080/00107514.2024.2423496`.

[13] Chiara Caprini et al. “Gravitational waves from first-order phase transitions in LISA: reconstruction pipeline and physics interpretation”. In: *JCAP* 10.020 (2024). DOI: `10.1088/1475-7516/2024/10/020`.

[14] Joseph Simon and the NANOGrav Collaboration. “Searching for the stochastic gravitational-wave background with the NANOGrav 15-year dataset”. In: *arXiv preprint* (2023). arXiv: `2306.16219 [astro-ph.HE]`. URL: `https://arxiv.org/abs/2306.16219`.

[15] Emmy Noether. “Invariante Variationsprobleme”. de. In: *Nachrichten von der Gesellschaft der Wissenschaften zu Göttingen, Mathematisch-Physikalische Klasse* 1918 (1918), pp. 235–257. URL: `https://eudml.org/doc/59024`.

[16] Curtis G. Callan and Sidney R. Coleman. “Fate of the False Vacuum. II. First Quantum Corrections”. In: *Phys. Rev. D* 16 (1977), pp. 1762–1768. DOI: `10.1103/PhysRevD.16.1762`.

[17] Sidney R. Coleman. “The Fate of the False Vacuum: Semiclassical Theory”. In: *Phys. Rev. D* 15 (1977), pp. 2929–2936. DOI: `10.1103/PhysRevD.15.2929`.

[18] Mark B. Hindmarsh et al. “Phase transitions in the early universe”. In: *SciPost Phys. Lect. Notes* 24 (2021). DOI: `10.21468/SciPostPhysLectNotes.24`.

[19] Michele Maggiore. *Gravitational Waves: Volume 1: Theory and Experiments*. Vol. 1. Oxford: Oxford University Press, 2008.

[20] Albert Einstein. “Approximative integration of the field equations of gravitation”. In: *Sitzungsber. Preuss. Akad. Wiss. Berlin (Math. Phys.)* 1916 (1916). In German, pp. 688–696. URL: `https://inspirehep.net/literature/42612`.

[21] Albert Einstein. “Über Gravitationswellen”. In: *Sitzungsber. Preuss. Akad. Wiss. Berlin* 1918 (1918). In German, pp. 154–167. URL: `https://cds.cern.ch/record/632352`.

[22] Glauber C. Dorsch and Lucas E. A. Porto. “An introduction to gravitational waves through electrodynamics: a quadrupole comparison”. In: *European Journal of Physics* 43.2 (2022), p. 025501. DOI: `10.1088/1361-6404/ac4645`.

[23] R. W. Hellings and G. S. Downs. “Upper Limits on the Isotropic Gravitational Radiation Background from Pulsar Timing Analysis”. In: *Astrophysical Journal* 265 (Feb. 1983), pp. L39–L42. DOI: `10.1086/183954`.

[24] Peter Athron et al. “Cosmological phase transitions: From perturbative particle physics to gravitational waves”. In: *Progress in Particle and Nuclear Physics* 135 (2024), p. 104094. ISSN: 0146-6410. DOI: `10.1016/j.ppnp.2023.104094`. URL: `http://dx.doi.org/10.1016/j.ppnp.2023.104094`.

[25] Arthur Kosowsky, Michael S. Turner, and Richard Watkins. “Gravitational radiation from colliding vacuum bubbles”. In: *Phys. Rev. D* 45.12 (1992),

pp. 4514–4535. DOI: 10.1103/PhysRevD.45.4514. URL: https://doi.org/10.1103/PhysRevD.45.4514.

[26] Andrea Mitridate et al. “PTArcade”. In: *arXiv preprint arXiv:2306.16377* (2023). DOI: 10.48550/arXiv.2306.16377. URL: https://arxiv.org/abs/2306.16377.

[27] J. A. Ellis et al. *ENTERPRISE: Enhanced Numerical Toolbox Enabling a Robust Pulsar Inference SuitE*. Astrophysics Source Code Library, ascl:1912.015. 2019. URL: https://ascl.net/1912.015.

[28] S. R. Taylor et al. *enterprise_extensions*. Version 2.3.3, GitHub repository. 2021. URL: https://github.com/nanograv/enterprise_extensions.

[29] W. G. Lamb, S. R. Taylor, and R. van Haasteren. “The need for speed: Rapid refitting techniques for Bayesian spectral characterization of the gravitational wave background using PTAs”. In: *arXiv preprint* arXiv:2303.15442 (2023). URL: https://arxiv.org/abs/2303.15442.

[30] S. J. Huber and T. Konstandin. “Gravitational Wave Production by Collisions: More Bubbles”. In: *JCAP* 09.022 (2008). DOI: 10.1088/1475-7516/2008/09/022. eprint: 0806.1828.

[31] A. Kosowsky and M. S. Turner. “Gravitational radiation from colliding vacuum bubbles: envelope approximation to many bubble collisions”. In: *Phys. Rev. D* 47 (1993), pp. 4372–4391. DOI: 10.1103/PhysRevD.47.4372. eprint: astro-ph/9211004.

[32] Mark Hindmarsh and Mulham Hijazi. “Gravitational waves from first order cosmological phase transitions in the Sound Shell Model”. In: *Journal of Cosmology and Astroparticle Physics* 2019.12 (2019), pp. 062–062. ISSN: 1475-7516. DOI: 10.1088/1475-7516/2019/12/062. URL: http://dx.doi.org/10.1088/1475-7516/2019/12/062.